

Theory of two-electrons optics experiments with smooth potentials: Flying electron molecules

P. G. Silvestrov,¹ Vyacheslavs Kashcheyevs,² and Patrik Recher^{1,3}

¹*Institut für Mathematische Physik, Technische Universität Braunschweig, D-38106 Braunschweig, Germany*

²*Department of Physics, University of Latvia, Riga, LV-1004, Latvia*

³*Laboratory for Emerging Nanometrology Braunschweig, D-38106 Braunschweig, Germany*

Recent experimental progress in development of on-demand sources of electrons propagating along depleted quantum Hall edge channels has enabled creation and characterization of sufficiently compact single- and two-electron distributions with picosecond scale control and the possibility of measuring details of these distributions. Here, we consider the effects of the long-range Coulomb interaction between two electrons on the real time evolution of such distributions in the experimentally relevant case of smooth guiding and quantum point contact (QPC) potentials. Both Hanbury Brown and Twiss (HBT) and Hong-Ou-Mandel (HOM) setups are investigated. The theoretical consideration takes advantage of the separation of degrees of freedom leading to the independent motion of the center of mass and the relative motion. The most prominent effect of this separation is the prediction of molecular bound states, into which two electrons can become trapped and propagate as a pair along the center of mass trajectory while simultaneously rotating around each other. The existence of a number of such molecular bound states should naturally strongly affect the outgoing electrons' distribution in the HBT experiment leading to bunching. But also in the HOM setup where colliding electrons are initially spatially separated, we predict new effects due to the quantum tunneling of two electrons colliding at the QPC into the joint molecular bound states. The lifetime of these quasi-bound states is shown to depend on the symmetry of the orbital wave function of the two-electron state giving rise to means to distinguish spin-triplets from spin-singlets (enabling the creation of electronic Einstein-Podolsky-Rosen (EPR) pairs). As a characteristic signature of the paired states we investigate the probability for both injected electrons to stay a long time at the QPC.

I. INTRODUCTION

The field of electron quantum optics aims at developing control of quantum transport experiments using setups and approaches of photonic quantum optics [1, 2]. Static electron sources connected to quantum Hall edge channels could demonstrate the Pauli exclusion principle in mesoscopic conductors [3, 4]. With the advent of time-dependent control over emission events [5], mesoscopic single-electron optics experiments became available. Signs of the exchange statistics of two electrons can be probed via scattering at beamsplitters in Hanbury Brown & Twiss (HBT) [6] and Hong-Ou-Mandel (HOM) [7] setups, similar to photons. Building on these developments, quantum tomography [8] of arbitrary excitations [9, 10] in a modulated Fermi sea of non-interacting electrons has been demonstrated. However, electrons are charged particles and so interaction effects have to be considered with exchange effects on equal footing in contrast to the case of photons. Another quantum property that naturally comes along with interacting particles is entanglement. Indeed it has been shown theoretically that the Coulomb interaction between electrons that collide at a beamsplitter can be employed for either creating [11–13] or detecting entanglement [14, 15]. A complementary regime for electron quantum optics with ballistic electrons isolated in energy, time and space from the parent 2D Hall system has emerged more recently [16–21], driven by the progress in generation and detection techniques for metrological on-demand electron sources [22–

24]. These techniques can generate particularly short in time (below 10 ps) and wide in energy (~ 1 meV) wave packets that can be interrogated using gate-defined partitioning barriers [17, 19, 25], including examination of partitioning of electron pairs in an HBT geometry [18] and demonstration of phase-space tomography for individual wave packets [26, 27]. Interaction effects between such isolated electrons have been recently scrutinized [15, 28–31] in the HOM geometry confirming effects of the strong Coulomb interaction.

In this work, we investigate the role of bound pair formation in the scattering at a beamsplitter in the lowest Landau level of quantized cyclotron motion. It is well known that in a strong magnetic field the repulsive Coulomb interaction allows for the formation of an anti-bound state of two electrons rotating around the center-of-mass [32]. This state is described by the two-electron limit of the celebrated Laughlin wave function [33] and is stable in the absence of disorder. We show that such pairs can not only survive in the presence of a smooth guiding- or beamsplitter potential (in the HBT geometry) but can actually be created (in the HOM geometry) out of initially separated electron pairs. We concentrate on energies for two electrons close to the top of a beamsplitter so that we can approximate it by a quadratic saddle point potential. We show that even with the mutual long-range Coulomb interaction, the dynamics separates exactly into a center of mass motion and a relative motion. We project the dynamics onto the lowest Landau level manifold assuming that the fast cyclotron motion

can be averaged over in favor of so called guiding coordinates x_g and y_g describing the drift motion in the smooth saddle point potential acting as a quantum point contact (QPC) [34]. In terms of x_g and y_g , the kinetic energy is completely quenched and only the potential energies and Coulomb interactions have to be kept, but now with x_g and y_g being conjugate variables $[x_g, y_g] = il_B^2$, where l_B is the magnetic length. Energy conservation of the two-particle system turns into contour lines of constant potential energy for the relative- and center of mass motion in phase space. We choose the distribution of energies of the emitted two electrons such that they follow a critical trajectory reaching (classically or semi-classically) the saddle point in the long-time limit. Crucially, for the relative motion, interactions split the single-electron saddle point into two interaction-induced ones, with a new region for bound motion in-between, see Figs. 2 and 3.

The general approach to the two-electron problem outlined in Sections II-III below has already been applied to the analysis of two-electron collisions [28–30]. In the work of Pavlovska *et al.* [28], we have solved the classical scattering problem in the HOM geometry and formulated analytic scaling relations for transmission thresholds. In the work of Ubbelohde *et al.* [29], these results were further developed into a fully analytical model for the analysis of counting statistics of scattering outcomes and estimation of key experimental parameters. The model was shown to correctly describe first and second order correlation signatures in the number of detected electrons as well as accurately predict the measured indicators of elastic energy exchange at near-coincident arrival. An independent development in Ref. 30 has deployed a numerical solution of the corresponding equations of motion [28] to analyze another experimental implementation of on-demand electron collisions, with convincing agreement between the model and the measurements. In this paper, we focus on two major ideas: scattering of anti-bound two-electron states (“molecules”, as outlined above), and universal time-domain behavior in a smooth beamsplitter potential.

In the *HBT geometry*, two electrons are considered to be paired into a bound state with the center of mass being that of a (rotating) molecule. In this case, we show that such molecules in the vicinity of the critical trajectory exhibit a universal long time tail $\sim e^{-\lambda t}$ for the pair to stay at the beamsplitter with λ being the Lyapunov exponent of the saddle point potential introduced precisely later. The decay rate of this probability only depends on the geometry of the beamsplitter potential (through λ) and is the same as it would be for a single electron and is therefore a direct test for the correlated two-particle pair to be bound into a molecule. Two independent electrons would show a more rapid decay of the probability to be simultaneously delayed at the beamsplitter as $\sim e^{-2\lambda t}$.

In contrast, in the *HOM geometry*, electrons are initially uncorrelated and the nearly critical trajectories are classically open visiting either one or both interacting saddle points for the relative coordinate before

they split apart. That leads to a modified long-time tail, $\sim \exp(-\lambda_I t)$ or $\sim \exp(-\lambda_I t/2)$, depending on whether the energy is below or above the critical level line. Here λ_I is the Lyapunov exponent of the interaction-induced saddle point and will be defined exactly below. Note that $\lambda_I > \lambda$ so that the center of mass and the relative coordinate distributions decay with different rates away from the center of the beamsplitter. Further, we consider the conditions on the two initial energies for the two electrons to visit the interacting saddle points as a function of their delay times and discuss the mechanism of energy exchange between the two electrons as measured experimentally [29]. Quantum mechanically, the relative coordinate can tunnel into molecular quasi-bound states of different orbital symmetries and lifetimes temporally separating singlet from triplet bound states. These features allow us to identify signatures of the beamsplitter potential, interaction effects and the formation of (possibly entangled) electron pairs in the time domain of electron quantum optics experiments. Time-resolved detection of individual propagating electrons in quantum Hall edge channels has become possible recently [19, 20, 26].

The structure of the paper is as follows. In Section II, we introduce our model of two interacting electrons in the presence of a strong magnetic field and subjected to a saddle point potential. In Section III, we demonstrate the exact separation of the center of mass from the relative motion and switch to the relevant and canonically conjugate guiding center coordinates describing the drift motion of the two electrons in the saddle point potential. In Section IV, we discuss the effects of a quadratic saddle point potential on the energy-time and the time distributions, using a phase-space picture that allows for the representation of quantum scattering dynamics in terms of an ensemble of classical trajectories under a Liouvillian flow. The results apply equally to scattering of a single electron and to the dynamics of the center of mass of an electron molecule. In both cases, a universal tail $\sim e^{-\lambda t}$ of the time distribution after passage through the beamsplitter is identified. Section V is devoted to analysis of the HOM geometry leading to a number of interdependent results. In Sec. VA, we discuss the role of exchange symmetry on the initial conditions and the corresponding Wigner representations of the independently evolving relative and average coordinates, and examine universality of the late-time behavior of the two-electron quantum state at the beamsplitter. Next (Section VB), we examine the classical dynamics of the centers of sufficiently localized distributions, focusing on two special cases that admit a simple analytical treatment and an intuitive discussion of the associated interplay of energy and time differences between the two electrons. Section VC introduces a simple model Hamiltonian to describe dynamics near the two interacting-induced saddle points, and illustrates the key quantum effects of resonant formation and a slow decay of the bound-pair states at the beamsplitter. Finally, in Section VD we discuss how the universal delay at the beamsplitter and the parity

selection rule for the resonant wave functions could be used to filter entangled Einstein-Podolsky-Rosen (EPR) pairs. A short conclusion in Section VI completes the paper.

II. INTERACTING ELECTRONS IN A SMOOTH POTENTIAL.

Propagation of two electrons is described by the Hamiltonian

$$H = h(\mathbf{r}_1) + h(\mathbf{r}_2) + \frac{e^2}{\kappa r}. \quad (1)$$

Here $r = |\mathbf{r}_1 - \mathbf{r}_2|$, $\kappa = 4\pi\epsilon_0\epsilon_r$ is the dielectric constant and

$$h(\mathbf{r}) = \frac{\mathcal{P}_x^2}{2m} + \frac{\mathcal{P}_y^2}{2m} + V(x, y), \quad [\mathcal{P}_x, \mathcal{P}_y] = i\hbar eB, \quad (2)$$

with $V(x, y)$ the confining potential and m the effective mass. The magnetic field $B = B_z$ enters this formula via the commutation relation of \mathcal{P}_x and \mathcal{P}_y which is independent of the specific gauge of the vector potential. For GaAs, the effective mass $m = 0.067 m_e$, and the relative dielectric constant $\epsilon_r = 12$, where m_e is the electron mass in the vacuum.

The smooth potential $V(x, y)$ defines the lateral confinement of electrons. It is shown in Fig. 1, how both HBT- and HOM-electron setups may be realized in a wide wire ($V(x, y) \approx C'y^2/2 + \text{const}$) interrupted by a smooth potential barrier. On-demand electron sources S_1 and S_2 can inject electron wave packets from opposite sides, and detectors D_1 and D_2 are used to resolve the scattering outcome. The center of the barrier potential contains a saddle point, where one can write [35]

$$V(x, y) \approx V_0 - \frac{Ax^2}{2} + \frac{Cy^2}{2}. \quad (3)$$

For electrons with energies close to V_0 this potential works as a quantum point contact or a beamsplitter. We will mostly use V_0 , which corresponds to the single electron half-transmission energy, as zero energy, i.e. $V_0 \equiv 0$.

For the transverse magnetic field $B = 14$ T typical in the experiments [20] the magnetic length $l_B = \sqrt{\hbar/eB} \approx 6.86$ nm is naturally small compared to the scale of variation of the confining potential $V(x, y)$. In this case, the electron's dynamics (either classical, or quantum) may be adequately described by the Born-Oppenheimer approximation separating fast (cyclotron rotation) and slow (drifting of the cyclotron guiding centers) degrees of freedom. The cyclotron motion of each electron in the experiments with strong magnetic fields is always quantized and to a good approximation we may assume working in the subspace of the Hilbert space formed by the $N = 0$ Landau level electrons only. In this case the dynamics of two electrons guiding centers is quantitatively described

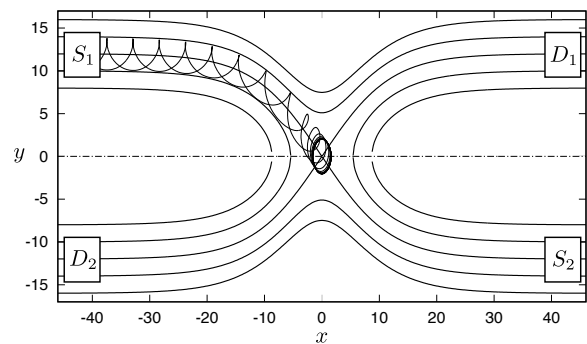


FIG. 1. Experimental setup: HBT/HOM electron optics setup. We show the constant energy lines for the potential $V(x, y)$ defining a wide quantum wire interrupted by a saddle-point QPC. Non-interacting electrons can drift along these lines from either of the sources S_1, S_2 to one of the detectors D_1, D_2 . Also shown is the example of the classical trajectories of a pair of interacting electrons entering the beamsplitter from the source S_1 and staying there forever (conditions for this singular case are discussed in the text).

by the effective Hamiltonian

$$H_{\text{eff}} = \hbar\omega_L + V(x_1, y_1) + V(x_2, y_2) + \frac{e^2}{\kappa|\mathbf{r}_1 - \mathbf{r}_2|}, \quad (4)$$

where now the coordinate operators obey the commutator relations [36]

$$[x_i, y_j] = i\hbar_{\text{eff}} \delta_{ij} = il_B^2 \delta_{ij}. \quad (5)$$

The kinetic energy of two electrons in the magnetic field $\mathcal{P}^2/(2m)$ became a trivial constant in the effective Hamiltonian Eq. (4), $\mathcal{P}_1^2/(2m) = \mathcal{P}_2^2/(2m) = \hbar\omega_L/2 = \hbar eB/(2m)$, which accounts for the electrons' energies in the lowest Landau level.

In a similar fashion, we may introduce the effective Hamiltonian describing the motion of a single electron in the confining potential $V(x, y)$

$$H_{\text{eff}}^{(1)} = \hbar\omega_L/2 + V(x, y). \quad (6)$$

Here, the guiding center coordinates x and y are canonically conjugated variables as in Eq. (5), which means that the Hamiltonian $H_{\text{eff}}^{(1)}$ describes a one-dimensional problem with *e.g.* the “coordinate” x and the “momentum” y . Classical drifting trajectories for such a problem are the equipotential contours, $V(x, y) = \text{const}$, which we show in Fig. 1 for the wire-barrier interferometer.

The saddle point $x = 0, y = 0$ in Fig. 1 is the point where the topology of the trajectories changes. The two straight-line trajectories here are the separatrix trajectories. There the particles approach (leave) the unstable stationary trajectory $(x(t), y(t)) = (0, 0)$ exponentially in time. These trajectories correspond to half transmission in the quantum mechanical case. They are the only classical trajectories with indeterminate scattering outcome.

For a smooth potential $V(x, y)$, the use of the classical approximation is parametrically justified as long as one is not interested in any features on an area smaller than l_B^2 .

Classical equations of motion for the guiding centers coordinates of two electrons follow from the effective Hamiltonian Eqs. (4,5)

$$\dot{x}_i = \frac{l_B^2}{\hbar} \frac{\partial H_{\text{eff}}}{\partial y_i} = \frac{1}{eB} \frac{\partial H_{\text{eff}}}{\partial y_i}, \quad \dot{y}_i = -\frac{1}{eB} \frac{\partial H_{\text{eff}}}{\partial x_i}. \quad (7)$$

These equations may serve as a starting point for numerical investigations of two-electron transport. Now in Fig. 1, we show a typical example of the trajectories $\mathbf{r}_1(t)$ and $\mathbf{r}_2(t)$ of two interacting electrons with close starting points $\mathbf{r}_1(0)$ and $\mathbf{r}_2(0)$. Formally, drawing two trajectories on a plane does not give a true insight into the dynamics due to the lack of information about the temporal synchronization of $\mathbf{r}_1(t_1)$ and $\mathbf{r}_2(t_2)$. Nevertheless, by looking at the trajectories in Fig. 1 we can conjecture the coherent motion of some rotating extended combined ‘‘object’’. We will proceed in the next section with explaining the symmetry leading to this object.

III. SEPARATION OF VARIABLES

Separation of the Hamiltonian into parts depending on the relative coordinate and the center of mass position greatly simplifies the treatment of the problem of two interacting particles. In this section, we show how this decomposition helps us to describe the dynamics of two electrons in strong magnetic fields and smooth electrostatic potentials.

Transition to the relative and center of mass coordinates and momenta in the Hamiltonian Eqs. (1,2) is performed as

$$\begin{aligned} \mathbf{r} &= \mathbf{r}_1 - \mathbf{r}_2, \quad \mathbf{R} = (\mathbf{r}_1 + \mathbf{r}_2)/2, \\ \mathbf{p} &= (\vec{\mathcal{P}}_1 - \vec{\mathcal{P}}_2)/2, \quad \mathbf{P} = \vec{\mathcal{P}}_1 + \vec{\mathcal{P}}_2. \end{aligned} \quad (8)$$

This transformation leads to the desired decomposition of the kinetic energy as every two components of coordinate or canonical momentum referring to different electrons commute with each other.

Interaction between electrons is naturally only a function of the relative coordinate \mathbf{r} . Even more, in many cases of interest the potential $V(x_1, y_1) + V(x_2, y_2)$ also decouples into a sum of parts depending only on the center of mass or the relative coordinate.

The first of such an example is the motion in the uniform electric field, $V(x, y) = e\mathbf{E} \cdot \mathbf{r}$ with $|\mathbf{E}| = E$, where the Hamiltonian Eqs. (1,2) decouples as $H \equiv H_{\text{cm}}^E + H_{\text{r}}^E$ with

$$H_{\text{cm}}^E = \frac{\mathbf{P}^2}{2M} + 2e\mathbf{E} \cdot \mathbf{R}, \quad H_{\text{r}}^E = \frac{\mathbf{p}^2}{2\mu} + \frac{e^2}{\kappa r}. \quad (9)$$

Here $M = 2m$ and $\mu = m/2$ are the total and reduced masses, respectively. The first Hamiltonian H_{cm}^E , allowing for a simple exact solution, describes the drift

of a composite particle in a crossed electric and magnetic field. The drift velocity can be tuned by changing the emission energy at the source, with typical values of $v_d = E/B \approx (3 \dots 5) \cdot 10^4$ m/s at $B = 14$ T as reported in Ref. 20. The corresponding electric field may be characterized by the potential drop over the magnetic length, $l_B E \approx 4.8$ mV for $B = 14$ T and $v_d = 5 \cdot 10^4$ m/s.

The second Hamiltonian in Eq. (9) describes two electrons forming a two-dimensional anti-bound state in a magnetic field [32]. The presence of the Coulomb potential splits the degenerate Landau levels $N = 0, 1, \dots$ into

$$\mathcal{E}_n^N = \hbar\omega_L(N + 1/2) + \varepsilon_n^N. \quad (10)$$

Binding energies $-\varepsilon_n^N$ are negative due to the repulsive interaction and decrease with increasing n . For a strong quantizing magnetic field one may neglect the inter-Landau level transitions caused by the Coulomb interaction $e^2/(\kappa r)$. Eigenfunctions of H_{r}^E in this approximation coincide with the N -th Landau level states with given z -projection of angular momentum $m = n$ found in the symmetric gauge. For the $N = 0$ Landau level that we are interested in,

$$\varepsilon_n^0 = \frac{e^2}{\kappa l_B} \frac{\sqrt{\pi}(2n)!}{2^{2n+1}(n!)^2}. \quad (11)$$

For $B = 14$ T in GaAs we thus estimate the largest energy $\varepsilon_0^0 = \sqrt{\pi}e^2/(2\kappa l_B) = 12.3$ meV and the binding energies for $n \gg 1$,

$$\varepsilon_{n \gg 1}^0 = \frac{e^2}{2\kappa\sqrt{n}l_B} = \frac{6.9 \text{ meV}}{\sqrt{n}}. \quad (12)$$

The energy gap between Landau levels is sufficiently large, $\hbar\omega_L = 24.4$ meV, and the reduction of the Hilbert space to $N = 0$ states works reasonably well even for $n = 0$ and becomes even better for large n .

The decomposition of the two-electron Hamiltonian Eq. (9) is exact as long as the electric field is uniform. For \mathbf{E} slowly changing spatially, Eq. (9) approximately still holds locally. This means that two electrons in a molecular state still drift as a whole with the center of mass retracing the equipotential line of $V(x, y)$. Here, slowly changing obviously means a small change experienced by a drifting molecule during one period of rotation.

For the anti-bound states with large n the period of rotation of two electrons around their center of mass is found as $d\varepsilon_n/dn = \hbar/T_n$ which equals to 3.5 meV/n^{3/2} for $B = 14$ T, leading to $T_n = 0.019 \times n^{3/2}$ ps. The two electrons rotate around their center of mass at a distance $|\mathbf{r}_1 - \mathbf{r}_2|/2 = \sqrt{n}l_B$ with the velocity $v_n = (2.27/n) \times 10^6$ m/s. That means that for the edges investigated in Ref. [20], the velocity of the mutual rotation of the electron pair equals to the center of mass drifting velocity only for $n \approx 50$. For molecular states with such large n deviations from the uniform electric field approximation Eq. (9) must be taken into account.

Considering nonuniform in-plane electric fields is done by adding to the potential $V(x, y) = e\mathbf{E} \cdot \mathbf{r}$ the terms quadratic in coordinates. Remarkably, due to the symmetry with respect to electrons permutation the quadratic part of the full potential $V(x_1, y_1) + V(x_2, y_2)$ still decouples exactly into a sum of quadratic parts in either relative and center of mass coordinate.

It will be enough for us to consider the quadratic potential of the QPC Eq. (3), for which one readily finds the Hamiltonians ($H = H_{\text{cm}} + H_{\text{r}}$) of the center of mass

$$H_{\text{cm}} = \frac{\mathbf{P}^2}{2M} - AX^2 + CY^2, \quad (13)$$

$$H_{\text{cm}}^{\text{eff}} = \frac{\hbar\omega_L}{2} - AX_g^2 + CY_g^2,$$

and the relative motion

$$H_{\text{r}} = \frac{\mathbf{p}^2}{2\mu} - \frac{Ax^2}{4} + \frac{Cy^2}{4} + \frac{e^2}{\kappa r}, \quad (14)$$

$$H_{\text{r}}^{\text{eff}} = \frac{\hbar\omega_L}{2} - \frac{Ax_g^2}{4} + \frac{Cy_g^2}{4} + \frac{e^2}{\kappa r_g}.$$

Here, the subscript “g” labels the guiding center coordinates. Eqs. (13,14) with arbitrary coefficients A and C describe the dynamics of two electrons in the most generic quadratic potential. Only for $A, C > 0$ they describe the saddle point potential. Another important case $A = 0, C > 0$ is a wide wire having a parabolic confinement and dispersive edge states on each side with the drift velocity varying with electron’s energy. Both parameter regimes appear in the setup sketched in Fig. 1, where wide wire-like sections are interrupted by the barrier implemented as a saddle-point potential.

The decomposition $H = H_{\text{cm}} + H_{\text{r}}$, Eqs. (13) and (14), is exact. In a strong quantizing magnetic field, each of the two Hamiltonians H_{cm} and H_{r} describes the fast cyclotron rotation of the corresponding coordinate followed by a slow drift of the circular orbit’s guiding center (X_g, Y_g) or (x_g, y_g). Similarly to Eqs. (4,5,6), we may assume that the cyclotron rotation is taken care of by the Landau quantization involving the large gap $\hbar\omega_L$ and we may introduce the separate effective Hamiltonians $H_{\text{cm}}^{\text{eff}}$ and $H_{\text{r}}^{\text{eff}}$. This is done (as we have already shown in Eqs. (13,14)) by replacing

$$\mathbf{P}^2/(2M) \rightarrow \hbar\omega_L/2, \quad \mathbf{p}^2/(2\mu) \rightarrow \hbar\omega_L/2, \quad (15)$$

meaning that both fast rotational degrees of freedom are in the ground state ($N = 0$). The coordinates X, Y, x, y become now the operators of the guiding centers positions satisfying the commutation relations [36], cf. Eq. (5),

$$[X_g, Y_g] = i l_B^2/2, \quad [x_g, y_g] = i 2l_B^2. \quad (16)$$

We will consider mostly the guiding centers dynamics in the following and omit the subscript g consequently. Numerical coefficients on the *r.h.s.* of the equalities Eq. (16) are different because of the transformation to the center

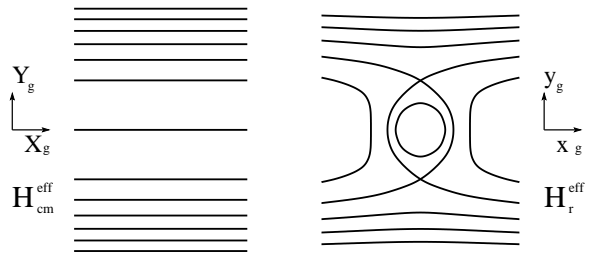


FIG. 2. Contour plot for the effective Hamiltonian $H_{\text{cm}}^{\text{eff}}(X_g, Y_g)$ Eq. (13) and $H_{\text{r}}^{\text{eff}}(x_g, y_g)$ Eq. (14) for $A = 0$ describing the dynamics of the center of mass and relative coordinate guiding centers of two electrons in a wide quantum wire.

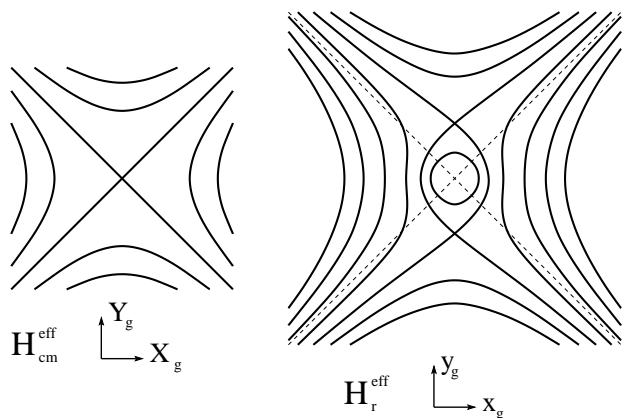


FIG. 3. Contour plot for the effective Hamiltonian $H_{\text{cm}}^{\text{eff}}(X_g, Y_g)$ Eq. (13) and $H_{\text{r}}^{\text{eff}}(x_g, y_g)$ Eq. (14) for $A = C$ describing the dynamics of the center of mass and relative coordinate guiding centers of two electrons in a beamsplitter configuration.

of mass and relative coordinates, Eq. (8), not being unitary.

Importantly, the electron-electron interaction is absent in the center of mass Hamiltonian H_{cm} , Eq. (13) (as well as in H_{cm}^{E} , Eq. (9)). That means that the dynamics of the pair’s center of mass coincides with the dynamics of a single electron with the same initial conditions (think of the motion of a pair of non-interacting electrons moving with negligible displacement). The motion of the center of mass separates into the fast cyclotron rotation and the slow drift of the center of this rotation along the lines of constant energy of the effective Hamiltonian $H_{\text{cm}}^{\text{eff}}$, Eq. (13), which in turn coincide with the equipotential lines of $V(x, y)$. The cyclotron motion of the center of mass is quantized and hence is considered in the lowest Landau level only, with constant kinetic energy Eq. (15).

A. Drift motion of the center of mass of two electrons in a dispersive edge

Consider now in more details the case of the pair of electrons in a single dispersive edge. As we discussed already, an adequate model for such an edge is a wide wire described by Eqs. (13,14) with $A \equiv 0$ and a parabolic transverse confinement potential $V(x, y) \sim y^2$. The topographic map for the effective Hamiltonian for the center of mass $H_{\text{cm}}^{\text{eff}}$, Eq. (13), in this case, shown in Fig. 2 (left panel), consists of a set of straight lines $Y_g = \text{const.}$ The distance between lines is inversely proportional to $|Y_g|$ and the drift velocity is linear in the coordinate $v_{x_{\text{cm}}} = CY_g$.

The curvature C of the electric potential along the depleted edge has been estimated experimentally from time-of-flight measurements [20] and from the energy dependence of LO phonon emission [37]. Reported values are $\hbar\omega_y = \hbar\sqrt{C/m} = 1.8 \text{ meV}$ to 2.7 meV [20] and $\hbar\omega_y = 2.7 \text{ meV}$ [29], and may vary depending on the sample and fabrication details.

B. Drift motion of the relative coordinate of two interacting electrons in a dispersive edge

The situation of the relative coordinate Eq. (14) is more involved. The guiding center drifts along the constant energy lines of the effective Hamiltonian $H_r^{\text{eff}}(x, y)$, which now becomes a sum of the wire potential $V(x, y) = Cy^2/4$ and the electrons' repulsion $e^2/(\kappa r)$.

The topographic map of the effective Hamiltonian $H_r^{\text{eff}}(x_g, y_g)$, Eq. (14), with $A = 0$ is shown in Fig. 2 (right panel). The new feature of this map is the existence of two interaction induced saddle points with $(x_g, y_g) = (0, \pm y_0)$ and the finite region of closed trajectories/equipotential lines between them. The area included inside the allowed trajectories is quantized in units of $4\pi l_B^2$ according to Eq. (16).

For the edge with no velocity dispersion, Eq. (9), the spectrum of two electron states is discrete with the excitation energies given by Eq. (11). As we see, for the dispersive edge with the concave edge potential ($C > 0$) the total number of possible molecular bound states is finite.

From the effective Hamiltonian $H_r^{\text{eff}}(x_g, y_g)$, Eq. (14), one easily finds the coordinate of the saddle point $y_0 = (2e^2/(\kappa C))^{1/3}$. The total area covered by the periodic trajectories is $A_{\text{mol}} = 2y_0^2(3 - 2\ln 2)/\sqrt{3} \approx 1.86y_0^2$. Parameters of the experiment analyzed in Ref. 29 are $y_0 = 45 \text{ nm}$ and $l_B = 8 \text{ nm}$ at $B = 10 \text{ T}$, hence we estimate $y_0 \approx 5.6l_B$ and the total number of distinct molecular states $N_{\text{mol}} = A_{\text{mol}}/(4\pi l_B^2) = 4.6$. The number of molecular states is sufficiently large to justify the use of a (semi)classical approach, but not large enough to make quantum effects, like quantum tunneling, invisible.

In the experimental devices the curvature of the edge potential (C in our notations) may vary along the edge.

Even more, typically in one and the same device there are two kinds of edges, produced by etching the 2DEG and by the electron repulsion from the metallic gates. So far, we considered the case of a concave edge potential, $C > 0$. It may easily happen (or may be designed on purpose) that at least a part of the drifting trajectory will traverse a region with a convex edge potential, i.e. $C < 0$. All the trajectories for the relative coordinate $\mathbf{r}(t)$ in such a region are closed and all two-electron states are (at least weakly) bound molecules.

C. Drift motion of the center of mass of two interacting electrons in the saddle point potential

Our next step is to consider the electron's pair dynamics in the saddle-point potential $V(x, y) = -Ax^2/2 + Cy^2/2$, Eq. (3). Since the potential is quadratic in coordinates, there is an exact separation of the Hamiltonian into the center of mass H_{cm} , Eq. (13), and the relative coordinate H_r , Eq. (14), parts.

The center of mass Hamiltonian H_{cm} is fully quadratic in both coordinates and momenta and as such can be solved exactly [34]. This solution consists of another exact decomposition of H_{cm} into a sum of two quadratic one-dimensional Hamiltonians each with its pair of canonically conjugated variables. These pairs of variables are the (canonically conjugated) coordinates of the cyclotron rotation of the center of mass and (also canonically conjugated) coordinates of the drifting center of this rotation. In the limit of a strong quantizing magnetic field, which is our focus here, the cyclotron rotation is projected to the $N = 0$ Landau level, which is reflected by the constant $\hbar\omega_L/2$ term in the effective guiding center Hamiltonian $H_{\text{cm}}^{\text{eff}}$, Eq. (13). Classical trajectories for the center of mass guiding center motion, which are the lines of constant energy $H_{\text{cm}}^{\text{eff}}(X_g, Y_g) = \text{const}$ are shown in Fig. 3 (left panel). For the pure quadratic Hamiltonian these trajectories are hyperbolas with the separatrix trajectories being straight lines. At the origin, there is a single unstable stationary trajectory $(X_g(t), Y_g(t)) \equiv (0, 0)$.

Later in the paper we will often refer to the classical trajectories for the Hamiltonians Eqs. (13,14). For the center of mass Hamiltonian $H_{\text{cm}}^{\text{eff}}$ with the commutation relations Eq. (16) one easily derives the classical equations of motion leading to the two-parameter family of trajectories

$$X_g = \frac{\alpha e^{-\lambda t}}{\sqrt{A}} + \frac{\beta e^{\lambda t}}{\sqrt{A}}, \quad Y_g = \frac{\alpha e^{-\lambda t}}{\sqrt{C}} - \frac{\beta e^{\lambda t}}{\sqrt{C}}. \quad (17)$$

Here $\lambda = l_B^2 \sqrt{AC}/\hbar = (1/eB)\sqrt{AC}$ is the classical Lyapunov exponent. Taking α and β to be very small leads to trajectories that stay long at the unstable stationary point. Quantitative modelling of the HOM-type experiments [28] yields $\lambda^{-1} \approx 2 \text{ ps}$ [30] to $\approx 4 \text{ ps}$ [29].

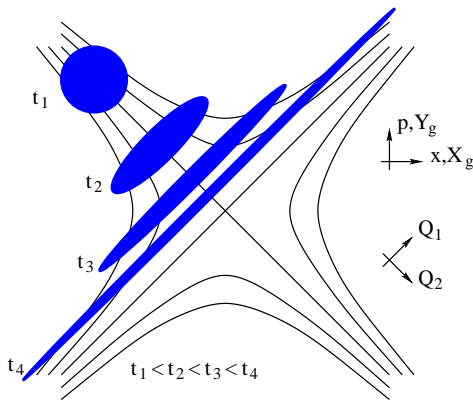


FIG. 4. Time evolution of a compact distribution of a particle on the (x, p) plane in the vicinity of the parabolic potential barrier Eq. (19). This may either refer to the evolution of the classical probability density, or the density described by the Wigner function for a quantum mechanical wave packet.

D. Drift motion of the relative coordinate of two interacting electrons in the saddle point potential

The topographic map of the effective Hamiltonian $H_r^{\text{eff}}(x_g, y_g)$ of the relative coordinate, Eq. (14), which illustrates possible classical trajectories described by this Hamiltonian and for a case of the beamsplitter potential Eq. (3) is shown in Fig. 3b. Similar to the case of the dispersive edge, Fig. 2b, the map shows two interaction induced saddle points at $(x_g, y_g) = (0, \pm y_0) = (0, \pm(2e^2/(\kappa C))^{1/3})$. Between them there is an area of periodic classical trajectories corresponding to long-lived quantum molecular states.

Classical solutions for the relative coordinate close to one of the interaction induced stationary points form a two parameter family (compare to the center of mass trajectories Eq. (17))

$$x_g = \frac{\gamma e^{-\lambda_I t}}{\sqrt{A+C}} + \frac{\delta e^{\lambda_I t}}{\sqrt{A+C}}, \quad y_g \mp y_0 = \frac{\gamma e^{-\lambda_I t}}{\sqrt{3C}} - \frac{\delta e^{\lambda_I t}}{\sqrt{3C}}, \quad (18)$$

where now $\lambda_I = (1/eB)\sqrt{3(A+C)C}$. These results are formally valid for $|x_g|, |y_g - y_0| \ll y_0$ or for $|x_g|, |y_g + y_0| \ll y_0$.

Since $\lambda_I > \lambda$, Eqs. (17, 18), in the vicinity of the double-stationary unstable point (stationary for both \mathbf{r}_g and \mathbf{R}_g) the relative coordinates trajectories diverge faster than the center-of-mass trajectories.

IV. HBT: DYNAMICS OF THE MOLECULE AT THE BEAMSPLITTER

In the previous section, we have shown that a pair of electrons in the QH edge may form an anti-bound state and travel together as a composite particle. Still, since in order to form a bound state electrons should be put close to each other, we expect the quantum wave packet

describing such joint propagation to be narrow in real space, ideally even narrow compared to the size of the beamsplitter. Such a situation can be naturally realized in HBT geometry if the electrons are injected by the source already as pairs.

In this section, we consider the transmission of a sufficiently short wave packet of such composite particles (molecules) through the beamsplitter described by the potential Eq. (3). Rather counterintuitively, the quantum tunneling dynamics of the wave packet turns out to be fully described in terms of classical mechanics. The main result of this section is the prediction of the universal long time probability to find the particle (*i.e.* two electrons together!) inside the device $\sim e^{-\lambda t}$, governed by the classical Lyapunov exponent λ .

The Hamiltonian describing the propagation of the composite particle through the beamsplitter takes the generic form

$$H_{\text{barrier}} = \frac{p^2}{2m} - \frac{m\lambda^2 x^2}{2}. \quad (19)$$

Comparing to $H_{\text{cm}}^{\text{eff}}$ via Eqs. (13, 16) one finds the translation rules: $x = X_g$, $p = 2\hbar Y_g/l_B^2$, $[x, p] = i\hbar$, $\lambda = l_B^2 \sqrt{AC}/\hbar = (1/eB)\sqrt{AC}$, $m = 2\hbar^2/(l_B^4 C) = 2(eB)^2/C$. In this notation, the classical Lyapunov exponent λ appears as an imaginary frequency of the conventional harmonic oscillator. Deviations from Eq. (19) in a smooth beamsplitter potential are expected to be small until some sufficiently large distances $x \sim L_{\text{barrier}} \gg \sqrt{\hbar/m\lambda} \sim l_B(C/A)^{1/4}$.

Scattering of a quantum particle on a potential barrier can be fully described by the transmission $t(\varepsilon)$ and reflection $r(\varepsilon)$ complex amplitudes. For a very mono-energetic wave packet with energy ε and extension long compared to the size of the scattering region $\Delta x \sim 1/\Delta p \gg L_{\text{barrier}}$, the wave packet propagates almost without dispersion and change of shape. Its scattering properties as *e.g.* transmission/reflection probabilities and delay times follow straightforwardly from $t(\varepsilon), r(\varepsilon)$. Short wave packets, $\Delta x < L_{\text{barrier}}$, are strongly deformed in the process of scattering (two electron propagation through a beamsplitter with interactions in the long wavepacket limit was considered in Ref. 15). Nevertheless, as we will see, for smooth potentials this deformation is still sufficiently universal and may be described by classical dynamics without referring to quantum scattering states. This is what we will discuss next.

A. Phase space dynamics of a bound molecule at the beamsplitter

Classical trajectories for the Hamiltonian Eq. (19) are linear combinations of exponential functions (see Eq. (17)). Now we are interested not in the motion of individual particles, but in the dynamics of an ensemble of particles. Let $\rho(x, p, t)$ be the distribution of the

ensemble. It may be a pure classical probability distribution originated from the limited accuracy of the initial particle parameters, or it may be a Wigner function corresponding to a quantum wave packet, with Weyl transform (Wigner representation) of the single-particle density matrix covering both cases (low-purity mixed state or a pure wave function, respectively) [27]. The exact time evolution of this distribution in phase space formulation of quantum mechanics [38] is described by its Moyal bracket with the Hamiltonian. For a polynomial Hamiltonian at most quadratic in x and p (such as H_{barrier} above) the Moyal bracket is identical with the Poisson bracket and hence the Wigner distribution follows the Liouvillian dynamics (classical Hamiltonian flow).

The properties of this flow are most easily revealed when viewed in a different system of coordinates determined by so called unstable and stable directions

$$Q_1 = \sqrt{\frac{m\lambda}{2}} x + \frac{p}{\sqrt{2m\lambda}}, \quad Q_2 = \sqrt{\frac{m\lambda}{2}} x - \frac{p}{\sqrt{2m\lambda}}. \quad (20)$$

Since the time dependence of these coordinates is purely exponential, $Q_1(t) = e^{\lambda t} Q_1(0)$, $Q_2(t) = e^{-\lambda t} Q_2(0)$, the time dependence of the density $\tilde{\rho}(Q_1, Q_2, t) = \rho(x(Q_1, Q_2), p(Q_1, Q_2), t)$ has a simple form

$$\tilde{\rho}(Q_1, Q_2, t) = \tilde{\rho}(Q_1 e^{-\lambda t}, Q_2 e^{\lambda t}, 0). \quad (21)$$

The evolution of an initially compact distribution described by Eq. (21) is shown in Fig. 4, which reveals the essence of scattering of distributions by the smooth barrier. In terms of individual classical trajectories, the parabolic barrier works as a perfect beamsplitter with all the trajectories with positive energy ($\varepsilon > 0$) being transmitted and all the trajectories with negative energy ($\varepsilon < 0$) being reflected. However, in terms of the evolution of a probability distribution, there is no splitting into two compact transmitted and reflected distributions. This is simply impossible in the case of the stretching and squeezing phase space dynamics within the beamsplitter region. If the average energy of the distribution is close to $\langle \varepsilon \rangle = 0$, all what one would see after a long time is an ensemble of particles sitting on the top of the barrier and uniformly (exponentially in time) expanding in both directions.

Importantly, although the behavior shown in Fig. 4 is purely classical, it describes correctly the evolution of the quantum mechanical Wigner function [39, 40], as we discussed above. The Wigner distribution carries the information about the quantum tunneling via the uncertainty principle as it contains a superposition of states both above and below the barrier [41]. Pursuing the line of reasoning similar to the one that led to Eq. (21) we find a more complicated formula relating the densities in phase space at times t and 0 in the original x and p coordinates

$$\begin{aligned} \rho(x_t, p_t, t) &= \rho(x_0(x_t, p_t), p_0(x_t, p_t), 0) \\ &= \rho(x_t c_\lambda - \frac{p_t s_\lambda}{m\lambda}, p_t c_\lambda - m\lambda x_t s_\lambda, 0), \end{aligned} \quad (22)$$

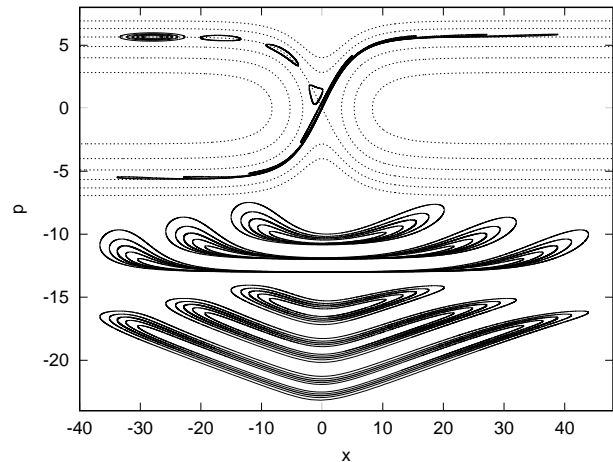


FIG. 5. Evolution of a classical particles distribution upon scattering on a realistic barrier modeled by the Hamiltonian $H_{\text{barrier}} = p^2/2 + A^2/\cosh(x/A)$, $A = 4$. The initial distribution is an asymmetric Gaussian centered at the incoming separatrix with the widths A in x -direction and $1/A$ in p -direction (this corresponds to a symmetric Gaussian distribution in the ε, t plane). One should remember that the classical Liouvillian evolution preserves the local densities and areas and that only the shapes of areas surrounded by the contour lines are deformed. **Top:** Distribution at the time slices $t = 0, 2, \dots, 14$ with the topographic map of the Hamiltonian shown in the background. The first, $t = 0$, distribution is shown by the contour lines at multiples of $1/6$ of the maximal density. For others only the $1/2$ -maximum contour is shown. **Middle:** At every point x the distribution at large times collapses to a single line – the outgoing separatrix $p_s(x)$, which for our model has a form $p_s(x) = 2A \sinh(x/2A)/\sqrt{\cosh(x/A)}$. Therefore, we show for the longest times, $t = 10, 12, 14$, the distribution of deviations from the limiting curve multiplied by 10 and offset downwards, $10 \times (p - p_s(x))$. The expanded vertical coordinate allows to show the full topographic map of the former Gaussian distribution with 5 slices of the density at $1/5$ of the maximum steps. **Bottom:** For the same large times probability density as a function of $\ln(p - p_s(x))$ and x showing the $e^{-\lambda t}$ tail of both reflected and transmitted distributions (offset downwards).

where $c_\lambda = \cosh \lambda t$ and $s_\lambda = \sinh \lambda t$. The coordinates x_t, p_t describe the particle at a time slice t and $x_0(x_t, p_t), p_0(x_t, p_t)$ is the initial point of the trajectory found as a function of the end-point. The expression Eq. (22) is still exact.

For direct comparison with the evolution of quantum mechanical wave packet it is convenient to introduce the classical density in the coordinate space

$$\rho(x, t) = \int \rho(x, p, t) dp. \quad (23)$$

Replacing integration over coordinates at current time t

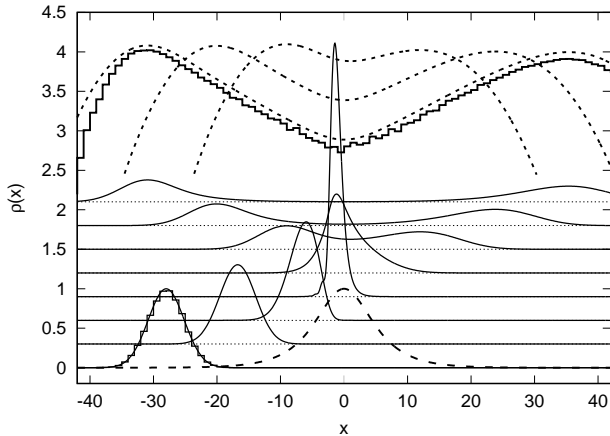


FIG. 6. Penetration of the short wave packet through the realistic smooth barrier at the half-transmission energy with the same model Hamiltonian as used for Fig. 5, $H_{\text{barrier}} = \hat{p}^2/2 + A^2/\cosh(x/A)$, $\hat{p} = -id/dx$, $A = 4$. The potential barrier is shown explicitly by the dashed line at the bottom (not in scale). Starting from the Gaussian wave packet $\psi_0 = \exp(-(x/A + 7)^2/2 + i\sqrt{2}Ax)$ we calculate the particle density $\rho_t(x) = |\psi_t(x)|^2$ for times $t = 0, 2, \dots, 14$. This is shown by solid black lines appropriately offset vertically. Short-dashed lines on the top show $\ln(\rho_t(x))/4$ (offset, divided by 4 for convenience) for the longest times $t = 10, 12, 14$. Results compare extremely well with the classical calculation in Fig. 5. To illustrate this, we show for the same classical Gaussian distribution as in Fig. 5 the distribution $p(x, t)$ defined in Eq. (23): histogram at the bottom-left shows $p(x, t = 0)$, histogram at the top shows $\ln(p(x, t = 14))/4$. The only “true quantum” effects visible in this figure are the small interference steps at the left wing of the sharpest peak $t = 6$.

by that at $t = 0$ we write

$$\begin{aligned} \rho(x, t) &= \int \delta(x - x_t) \rho(x_t, p_t, t) dx_t dp_t \\ &= \int \delta(x - x_t(x_0, p_0)) \rho(x_0, p_0, 0) dx_0 dp_0. \end{aligned} \quad (24)$$

From this we derive

$$\rho(x, t) = \int \rho\left(\frac{m\lambda x - p \sinh \lambda t}{m\lambda \cosh \lambda t}, p, 0\right) \frac{dp}{\cosh \lambda t}. \quad (25)$$

This formula is exact for the classical motion induced by the Hamiltonian Eq. (19). However, as long as the classical distribution is further stretched and becomes effectively one-dimensional, the particle inside the barrier is drastically simplified

$$\begin{aligned} \rho(x, t \gg 1/\lambda) &= e^{-\lambda t} f(e^{-\lambda t} x), \\ f(x) &= 2 \int \rho(2x - p/m\lambda, p, 0) dp. \end{aligned} \quad (26)$$

Here we introduced a scaling function f such that at large times $e^{\lambda t} \gg 1$ the evolution of the density reduces to a simple stretching of $f(x)$.

Formula (26) describes effectively the expansion in time of the mono-energetic distribution of the “chain” of particles. In Fig. 4 this corresponds to a line distribution for the long times along the unstable direction in phase space. The energy width of the initial distribution $\rho(x, p, 0)$ can be ignored since after long times, $t \gg 1/\lambda$, only the particles with negligibly small energies, $\varepsilon \approx 0$, are still present near the top of the barrier. Other particles by the time $t \gg 1/\lambda$ escape so far away from the $x \approx 0$ region that their energies may be ignored compared to the magnitude of the potential. Individual trajectories for particles constituting the distribution Eq. (26) have a simple exponential form

$$x(t) = x_0 e^{\lambda t}. \quad (27)$$

The accelerated exponential divergency of such trajectories, specific for the Hamiltonian Eq. (19) with bottomless reverse-parabolic potential, could not last forever. In a real system, the potential in Eq. (19) at some distance $|x| > L_{\text{barrier}}$ reaches a minimum and flattens. The particles after reaching this region continue to fly with the constant velocity $v \approx L_{\text{barrier}}\lambda$. Trajectory Eq. (27) for $x > L_{\text{barrier}}$ (or for $t > \ln(L_{\text{barrier}}/x_0)/\lambda$) transforms into

$$x(t) = L_{\text{barrier}} + v(t - \ln(L_{\text{barrier}}/x_0)/\lambda), \quad (28)$$

where the large logarithm is found up to a constant ~ 1 depending on the details how the barrier transforms from the parabolic top to the flat bottom.

The density distribution for particles (either reflected, or transmitted) described by Eq. (28) is related to the initial phase space density $\rho(x, p, 0)$ via the function $f(x)$ defined in Eq. (26) as

$$\rho(x, t) = (\lambda/v) R e^{(x-vt)\lambda/v} f(R e^{(x-vt)\lambda/v}), \quad (29)$$

where $R = \text{const} \times L_{\text{barrier}}$ with some model dependent constant of order unity.

In Fig. 5, we show the evolution of the classical distribution of particles found numerically for the realistic model barrier $V(x) = A^2/\cosh(x/A)$ supporting all the qualitative features of our theoretical picture. (Realistic here means a potential with a wide parabolic top, $L_{\text{barrier}} \sim A \gg 1$, Eq. (28), reaching a flat bottom $U = 0$ for $|x| \gg A$.) The figure shows how the compact Gaussian distribution approaching the potential barrier becomes effectively a single elongated line distribution collapsing to the separatrix trajectory $p_s(x)$ with the center pinned to the unstable stationary point. By plotting the displacement density on a logarithmic scale $x, p \rightarrow x, \ln(p - p_s(x))$ we show both – the flying head of the distribution Eq. (29) and the universal exponential tail.

Equation (29) shows the shape of the entire particle distribution after passing the beamsplitter. One may place a detector at some point x far away from the beamsplitter and measure the probability for the particle to be found there after a time t . At long times, the function f

in Eq. (29) saturates at $f(0)$. One expects here to measure the universal exponential tail of the rare events with large delay time $\sim e^{-\lambda t}$ with the exponent λ determined by the curvature of the potential barrier. We stress that this is the tail of the probability to find *both* electrons still in the beamsplitter.

B. Quantum mechanical treatment of a bound molecule at the beamsplitter

For a pure quantum mechanical ensemble, a uniformly decaying solution (26) of time evolution can also be obtained as a quasi-stationary solution to the time-dependent Schrödinger equation with the Hamiltonian Eq. (19) as

$$i\hbar\dot{\psi}_\lambda = H_{\text{barrier}}\psi_\lambda, \quad \psi_\lambda = e^{im\lambda x^2/\hbar - \lambda t/2}, \quad (30)$$

which is nothing more than the first quasi-stationary state in a parabolic potential with the imaginary energy $\varepsilon = i\hbar\lambda/2$. The density produced by this decaying quasi-stationary state $|\psi_\lambda|^2 = e^{-\lambda t}$ coincides with the classical density Eq. (26) for $xe^{-\lambda t} \ll 1$.

On the other hand, the classical distribution $\rho(x, p, t)$ for long times, when Eqs. (26,29) apply, becomes effectively a line in phase space. Such a density may be produced by a quantum mechanical wave function in the semiclassical approximation,

$$\psi(x, t) = \sqrt{\rho(x, t)} e^{iS(x, t)/\hbar}, \quad (31)$$

with an action S found from the classical Hamilton-Jacobi equation. $\psi(x, t)$ in Eq. (31) coincides with the quasi-stationary solution $\psi_\lambda(x, t)$ in Eq. (30) at distances $|x| \lesssim \sqrt{\hbar/m\lambda}$, where $S = m\lambda x^2$ and $\rho = e^{-\lambda t}$, even though the formal semiclassical expansion is not expected to be valid at such distances.

To illustrate the accuracy of the developed approximations for the wave packet propagation through the beamsplitter we performed fully quantum mechanical simulations for the barrier potential $V(x) = A^2/\cosh(x/A)$. The resulting density $\rho_t(x)$ as well as the logarithm of the density $\ln(\rho_t(x))$ are shown in Fig. 6.

We note that what is called in this section coordinate x and momentum p (either classical or quantum) become operators or expectation values of two (non-commuting) guiding center coordinates X_g and Y_g for the center of mass of the composite two-electron particle drifting in the strong magnetic field, described by the Hamiltonian $H_{\text{cm}}^{\text{eff}}$, Eq. (13).

The main result of this section is the prediction that for a generic ensemble of electrons approaching the beamsplitter with energies close to the pinch off, a fraction $\sim e^{-\lambda t}$ of the electron pairs will stay there for any long time t with the Lyapunov exponent λ determined by the curvatures of the potential barrier. If one would send two non-interacting electrons to the beamsplitter, the probability to find them both still inside the device decay much

faster, $\sim e^{-2\lambda t}$ since these are uncorrelated events. However, if the two electrons initially form a bound molecular state, which we introduced in the previous section, the probability for the pair to stay long at the QPC still decays in a single-particle way $\sim e^{-\lambda t}$.

V. HOM: QUANTUM TUNNELING INTO THE MOLECULE

Using the HOM setup offers an advantage compared to the HBT setup since colliding electrons from two independent sources enables greater degree of control over the incoming distributions [29, 30]. In this section, we describe the important theoretical aspects of the electron collision experiment at the beamsplitter, including the role of two-electron anti-bound states.

A. Long-time limit of two electron density at the beamsplitter

The space of parameters enumerating distinct classical scattering processes is three-dimensional as there are initial energies of the two electrons $i = 1, 2$, energies ε_1 and ε_2 , and the difference between the injection times, Δt_{in} . Interaction effects are obviously most relevant for the simultaneous injection, $\Delta t_{\text{in}} = 0$. Consequently, we start by considering two electron wave packets $\psi_1(x_i, t)$, $\psi_2(x_i, t)$ with energies $\approx \varepsilon_1, \approx \varepsilon_2$ injected simultaneously into the opposite arms of the beamsplitter, see Fig. 1.

We again are interested in the drift motion of the two electrons and consequently use guiding center coordinates x_i and y_i . However, only one of the electrons' non-commuting (see Eq. (5)) guiding-centers coordinates x_i or y_i may be treated as a canonical "coordinate". We so far have chosen the "coordinate" to be the "valley of the saddle" direction x , Eq. (3), which is the direction in which the current flows through the beamsplitter. Equivalence of the coordinates is restored if one considers the density defined in terms of the Wigner function

$$\rho_i(\mathbf{r}_j, t) = \frac{1}{\pi l_B^2} \int \psi_i^*(x_j + x'_j, t) \psi_i(x_j - x'_j, t) e^{2iy_j x'_j/l_B^2} dx'_j. \quad (32)$$

The two electrons injected into the beamsplitter are initially uncorrelated and described by an antisymmetrized product of their individual wave functions

$$\psi(x_1, x_2, t) = \frac{1}{\sqrt{2}} (\psi_1(x_1, t) \psi_2(x_2, t) - \psi_2(x_1, t) \psi_1(x_2, t)). \quad (33)$$

Here, we assume fully spin-polarized electrons and suppress the spin indices.

The corresponding density can be computed in analogy to Eq. (32) as

$$\rho(\mathbf{r}_1, \mathbf{r}_2, t) = \frac{1}{\pi^2 l_B^4} \iint \psi^*(x_1 + x'_1, x_2 + x'_2, t) \times \psi(x_1 - x'_1, x_2 - x'_2, t) e^{2i(y_1 x'_1 + y_2 x'_2)/l_B^2} dx'_1 dx'_2. \quad (34)$$

Describing electrons as independent in terms of coordinates x_1, x_2 in Eq. (33) works only at sufficiently early times, as long as the interaction may be neglected. This should be modified when the particles approach each other. As we discussed at length in Section III, in the region where the saddle point potential approximation Eq. (3) can be applied, the effective Hamiltonian for the guiding centres of the two electrons decouples into a sum of two Hamiltonians describing the motion of the center of mass, $H_{\text{cm}}^{\text{eff}}$ in Eq. (13), and the relative coordinate, H_r^{eff} in Eq. (14). Therefore, there exists a class of two-electron states in the beamsplitter region that remain a product of two independent wave functions at any time if expressed in terms of $x = x_1 - x_2$ and $X = (x_1 + x_2)/2$,

$$\psi(x_1, x_2, t) = \psi_r(x, t) \psi_{\text{cm}}(X, t), \quad (35)$$

where x and X are the relative and center-of-mass coordinates, respectively. Fermi statistics of spin-polarized electrons is accounted for by the symmetry condition $\psi_r(x, t) = -\psi_r(-x, t)$. Note that here x and X refer to guiding center coordinates of the relative and center of mass motion, respectively (i.e. $x \equiv x_g$ and $X \equiv X_g$).

The exact electron density in Eq. (34) in this case also factorizes ($\mathbf{r} = \mathbf{r}_1 - \mathbf{r}_2$, $\mathbf{R} = (\mathbf{r}_1 + \mathbf{r}_2)/2$)

$$\rho(\mathbf{r}_1, \mathbf{r}_2, t) = \rho_r(\mathbf{r}, t) \rho_{\text{cm}}(\mathbf{R}, t). \quad (36)$$

Here, the relative coordinate ρ_r and center of mass ρ_{cm} densities are found from the corresponding wave functions ψ_r and ψ_{cm} using Eq. (32) with l_B^2 replaced by $2l_B^2$ and $l_B^2/2$, respectively, to account for commutation relations (16). The exchange symmetry, $\psi_r(x, t) = \pm\psi_r(-x, t)$, implies $\rho_r(\mathbf{r}, t) = \rho_r(-\mathbf{r}, t)$, independent of the sign (which is ‘-’ in our case).

Solutions of the time dependent Schrödinger equation for the guiding centers of the form Eq. (33) and Eq. (35) may, but don’t have to coincide even for the large separation between electrons, where their interaction may yet be neglected. Nevertheless, there exists an interesting family of solutions for which the factorization Eq. (35) holds for the initial state Eq. (33) and hence is preserved during subsequent time evolution. Consider $\psi_i(x_i, t)$ as a Gaussian in x_i with some time-dependent, possibly complex, coefficients. A sum of two at most quadratic single-variable polynomials in x_1 and x_2 is equal to the sum of single-variable polynomials in x and X if and only if the coefficients in front x_1^2 and x_2^2 are equal. When this condition is true for $\ln\psi_i$, the initial state Eq. (33) factorizes with $\psi_r(x, t) = [\psi_1(x/2, t)\psi_2(-x/2, t) - \psi_1(-x/2, t)\psi_2(x/2, t)]/\sqrt{2}$ and $\psi_{\text{cm}}(X, t) = \psi_1(X, t)\psi_2(X, t)$. The initial wave function

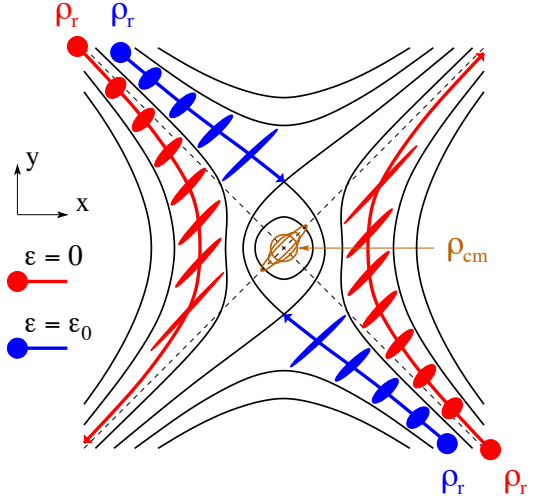


FIG. 7. Simultaneous injection of two Gaussian distributions of electrons in the HOM setup with energies ε close to 0 (red) and ε_0 (blue), cf. Eq. (39). The figure shows the central trajectories ($\varepsilon \equiv 0$, $\varepsilon \equiv \varepsilon_0$) and a schematic evolution of the distribution around them for the relative coordinate density $\rho_r(\mathbf{r}, t)$, Eq. (36). The solid black lines show the contour map of the effective Hamiltonian H_r^{eff} , Eq. (14). The evolution of the distribution of center of mass trajectories $\rho_{\text{cm}}(\mathbf{R}, t)$ is shown schematically in the center (brown). Since we consider the simultaneous equal-energies injection, the center of $\rho_{\text{cm}}(\mathbf{R}, t)$ stays at the stationary point $\mathbf{R}(t) \equiv 0$.

of the relative coordinate in this case is a cat state (superposition of well-separated Gaussians). If these incoming Gaussian wavepackets are also tuned to be symmetric with respect to the origin, $\psi_1(x, t) = \psi_2(-x, t)$, then $\psi_r(x, t) = [\psi_1^2(x/2, t) - \psi_1^2(-x/2, t)]/\sqrt{2}$ and $\psi_{\text{cm}}(X, t)$ is a Gaussian centered at the origin $X = 0$. The corresponding initial density ρ_r is a sum of two Gaussians (sans fine oscillations in ρ_r on the scale much smaller than l_B , which are characteristic to cat states and encode the sign of the exchange statistics) and ρ_{cm} is a Gaussian too. We will analyze in details the evolution of such a special distribution in Fig. 7.

In the most general case, the two-particle wave function in the beamsplitter region can be expressed via the multi-component generalization of Eq. (35)

$$\psi(x_1, x_2, t) = \sum_i c^i \psi_r^i(x, t) \psi_{\text{cm}}^i(X, t), \quad (37)$$

which is possible with some appropriate choice of $\psi_r^i, \psi_{\text{cm}}^i$ as Eq. (37) is a Schmidt decomposition of the two-electron state after the coordinate transformation. The separation of variables in the quadratic Hamiltonian ensures that the coefficients c^i are constants of motion.

The general wave function Eq. (37) simplifies drastically in the special interesting regime of long times and the center of mass coordinate X staying close to the top of the barrier. In this regime, individual center of mass

wave functions all behave like the quasi-stationary solution Eq. (30) discussed at the end of the previous section $\psi_{\text{cm}}^i(X, t) \rightarrow \delta^i \exp[im\lambda X^2/\hbar - \lambda t/2]$ with some coefficient δ^i . Thus effectively, here, Eq. (37) became a single product wave function Eq. (35) with

$$\begin{aligned} \psi_{\text{cm}}(X, t) &= e^{im\lambda X^2/\hbar - \lambda t/2}, \\ \psi_{\text{r}}(x, t) &= \sum_i c^i \delta^i \psi_{\text{r}}^i(x, t). \end{aligned} \quad (38)$$

Here, for the saddle point potential Eq. (3) and magnetic field B we have $m\lambda = 2(eB)\sqrt{A/C}$ and $\lambda = (1/eB)\sqrt{AC}$. This $\psi_{\text{cm}}(X, t)$ describes the longest surviving quasi-stationary state of the inverted parabolic potential, Eq. (30). Further evolution of the relative coordinate wave function $\psi_{\text{r}}(x, t)$ is governed by the effective Hamiltonian $H_{\text{r}}^{\text{eff}}$ Eq. (14), which we will consider later in Sec. VC.

B. Classical scattering at the beamsplitter

Having discussed the effective universality of the decomposition into the relative and center of mass coordinates, Eqs. (35, 36), we may now proceed with considering the interaction effects in the two-electron HOM experiment. In Fig. 7, we show (schematically) two small similar distributions $\rho_1(\mathbf{r}_1, t)$ and $\rho_2(\mathbf{r}_2, t)$ with the same mean energy $\varepsilon_1 = \varepsilon_2 = \varepsilon$ injected simultaneously through the opposite corners of the beamsplitter. In fact we show two pairs of such distributions — blue and red — for the reasons explained below. We assume that it is possible to create the distributions with the spatial dimensions small compared to the size of the beam splitter (L_{barrier} of the previous section).

For our first example, (red in Fig. 7) we placed the centers of both incoming electrons distributions ρ_1 and ρ_2 at the separatrix, which is the straight equipotential line of $V(x, y)$ separating the non-interacting single-electron trajectories with topologically different outcomes. For this choice the fate of the central trajectory of the wave packet/distribution is classically undetermined and effects of quantum mechanics became most pronounced. However, long-range interaction renders this former critical point for the relative coordinate of the two electrons trivial. Electrons' repulsion in the relative coordinate Hamiltonian increases the effective height of the barrier, from which the electrons are now simply reflected without spending much time inside the beamsplitter and thus not changing qualitatively their distribution. The process may be viewed as a classical particles anti-bunching with none of the electrons crossing the beamsplitter.

The new interaction-induced critical point is revealed if one raises the energy of incoming electrons such that they would be able to enter the beamsplitter and approach (asymptotically) the saddle point at $y = \pm y_0$ of the joint potential $V(x, y)/2 + e^2/(\kappa r)$. Corresponding trajectory

for the center of the electrons distribution is shown blue in Fig. 7.

The straightforward way to reach the critical point in the presence of the Coulomb interaction is to send two electrons simultaneously to the beamsplitter each with an extra energy

$$\varepsilon_0 = \frac{3(Ce^4/\kappa^2)^{1/3}}{4 \cdot 2^{1/3}}. \quad (39)$$

Here, C is the transverse curvature of the saddle point potential, Eq. (3), e is the electric charge and $\kappa = 4\pi\epsilon_0$ is the dielectric constant. The critical energy ε_0 , Eq. (39), is found as a half of the saddle-point energy of the effective Hamiltonian $H_{\text{r}}^{\text{eff}} - \hbar\omega_L/2$, Eq. (14), describing the relative coordinate $\mathbf{r} = \mathbf{r}_1 - \mathbf{r}_2$ dynamics. The value of $\varepsilon_0 = 3U/4$ where U parametrizes the Coulomb potential [28], $e^2/(\kappa r) = Uy_0/r$, in the experiment of Ref. 29 has been estimated to be about $\varepsilon_0 \approx 2$ meV.

If two electrons are sent to the beamsplitter with the time shift Δt_{in} , they still may stop at the same stationary critical point. However, the excess energy $2\varepsilon_0$ necessary to reach it must now be split unevenly between the electrons. Interestingly, in case of the sufficiently large saddle-point region, Eq. (3), the two energies $\varepsilon_1(\Delta t_{\text{in}})$ and $\varepsilon_2(\Delta t_{\text{in}})$ may be found analytically in a simple form

$$\varepsilon_1(\Delta t_{\text{in}}) = \frac{2\varepsilon_0}{1 + e^{\lambda\Delta t_{\text{in}}}}, \quad \varepsilon_2(\Delta t_{\text{in}}) = \frac{2\varepsilon_0}{1 + e^{-\lambda\Delta t_{\text{in}}}}. \quad (40)$$

Here, the pair's center of mass materially moves along its critical trajectory approaching the stationary point only asymptotically, which is not described by Fig. 7. Knowledge of $\varepsilon_1(\Delta t_{\text{in}})$, $\varepsilon_2(\Delta t_{\text{in}})$ allows us to find ε_0 , Eq. (39), and $\lambda = (1/eB)\sqrt{AC}$ and thus infer the curvatures of the saddle point A, C , Eq. (3).

For $\lambda\Delta t_{\text{in}} \gg 1$ the first electron in Eq. (40) is sent to the beamsplitter with the energy just marginally above the half-transmission and waits at the saddle point at the origin for the energetic partner from the other side. Then they relax at two emerging saddle points.

Derivation of Eq. (40) requires only the knowledge of electrons trajectories when they are well separated and don't interact (while both are already present inside the parabolic beamsplitter). The electrons' interaction enters this result only through the total electrons' energy $2\varepsilon_0$. The simple derivation of Eq. (40) is given in the Appendix. More generally, the classical scattering problem inside the saddle-point beamsplitter potential Eq. (3) can be reduced to quadratures [28, 29] for any combination of the incoming electron energies $\varepsilon_{1\text{in}}$ and $\varepsilon_{2\text{in}}$ and the incoming time shift Δt_{in} . Equation (40) can be seen as a special case of the analytic scaling relations [28] that map half-transmission thresholds from coincident arrival ($\Delta t_{\text{in}} = 0$) to a finite Δt_{in} .

As already discussed in the context of Fig. 7, the injection of two electrons at the non-interacting half-transmission energy $\varepsilon_{1\text{in}} = \varepsilon_{2\text{in}} = \varepsilon = 0$ is non-critical, *i.e.* there is no change of the trajectory topology upon

a small variation of initial conditions here. Nevertheless, the presence of the interaction leads to the interesting and potentially measurable effects for this choice of initial conditions (which can be tuned without synchronizing the sources). In Fig. 7, by red lines we show the trajectories for simultaneous ($\Delta t_{\text{in}} = 0$) injection of two $\varepsilon = 0$ electrons. Consider now, what happens if the two electrons are injected still both at $\varepsilon = 0$ but with a finite relative time delay Δt_{in} . In this setup we expect two clear signatures of interaction. First, for a pair of electrons each injected at non-interacting half-transmission but with a relative time delay, the center of mass does not stay at the stationary position $X, Y = 0$ of the Hamiltonian $H_{\text{cm}}^{\text{eff}}$ Eq. (13), but approaches it asymptotically at large times, $t \rightarrow \infty$. Thus the time delay between two electrons distributions measured after the reflection will be reduced, $\Delta t_{\text{out}} < \Delta t_{\text{in}}$, meaning electrons are effectively synchronized by the interaction (time domain bunching). Second, while the interaction tends to time-synchronize the electrons, they exchange the energy in an elastic collision, with the electron reaching the beamsplitter first (second) gaining (losing) energy.

Using the general solution for energy transfer [Eq. (26) of Supplementary note to Ref. 29] we can [42] compactly express the corresponding outgoing energies,

$$\varepsilon_{1\text{out}} = -\varepsilon_{2\text{out}} = \gamma_0 \varepsilon_0 \tanh(\lambda \Delta t_{\text{in}}/2), \quad (41)$$

where $\gamma_0 = 2[2A/(A+C)]^{1/3}/3$ is a dimensionless constant of order 1. The functional dependence of $\varepsilon_{1\text{out}}, \varepsilon_{2\text{out}}$ in Eq. (41) on Δt_{in} is derived in the Appendix, while finding the overall coefficient in Eq. (41) requires the methods used in [28]. We see that ε_0 given by Eq. (39) sets the typical scale of non-critical energy gain/loss for time separations Δt_{in} larger than the scale set by the inverse Lyapunov exponent λ^{-1} .

The corresponding synchronization effect can be quantified in terms of the time shift between the incoming and outgoing electrons, Δt_{in} and Δt_{out} , as defined by the asymptotics of the trajectories incoming from opposite sources and outgoing to the opposite detectors,

$$x_1(t)/x_2(t) = \begin{cases} -e^{-\lambda \Delta t_{\text{in}}}, & t \rightarrow -\infty \\ -e^{+\lambda \Delta t_{\text{out}}}, & t \rightarrow +\infty \end{cases}. \quad (42)$$

Using Eq. (20) of Ref. 28 for the asymptotics of outgoing trajectories, we obtain a compact relation

$$\tanh(\lambda \Delta t_{\text{out}}/2) = -\frac{\varepsilon}{2\gamma_0 \varepsilon_0} \sinh(\lambda \Delta t_{\text{in}}/2). \quad (43)$$

The r.h.s. of Eq. (43) vanishes for $\varepsilon = 0$ and remains a good approximation up to $|\varepsilon| \cosh(\lambda \Delta t_{\text{in}}/2) \lesssim \varepsilon_0 \gamma_0$. This implies that $|\Delta t_{\text{in}}|$ up to $\sim \lambda^{-1} \ln(\gamma_0 \varepsilon_0 / |\varepsilon|)$ can be compensated by interaction to achieve synchronization within the characteristic time λ^{-1} of the beamsplitter, $\Delta t_{\text{out}} \lesssim \lambda^{-1}$ [43].

In the examples above we have focused on the trajectories of the centers of sufficiently narrow statistical

distributions $\rho_{1(2)}$. In the latest experiments [29, 30] the uncertainty of the incoming energy and time distributions, as characterized by energy-time tomography [26] of the sources, was found to be comparable to the characteristic scales ε_0 and λ^{-1} of the interactions on the beamsplitter. Therefore, a statistical approach [29] averaging over classical outcomes [28] had to be developed for quantitative analysis of collision statistics. Both experiments [29, 30] have demonstrated capabilities relevant to the specific examples discussed in this subsection such as the ability to tune the relative delay $\langle \Delta t_{\text{in}} \rangle$ between the centers of the time distributions of the two electrons. In the experiment of Ref. 30, both electrons were kept at the same energy, while the height of the beamsplitter barrier was varied. In Ref. 29, the energy of one electron was kept at the non-interacting half-transmission, while the energy of the second injected electron was scanned.

A distinctive feature of the experiment by Ubbelohde et al. [29] is the access to full counting statistics of on-demand collision outcomes, including rare events when less than two electrons arrive at both detectors. As the energy relaxation during propagation along the edge of sample is sensitive to electron energy, the loss signal serves as a proxy for the energy gain or loss after an elastic collision at the beamsplitter, i.e. $\varepsilon_{1\text{out}} - \varepsilon_{1\text{in}} = -(\varepsilon_{2\text{out}} - \varepsilon_{2\text{in}})$. This loss signal has been measured and successfully modeled as function of Δt_{in} and $\varepsilon_{1\text{in}}$ in Ref. 29 (see Fig. 4 in the main text and Supplementary note VI). The reported agreement confirms the energy exchange effect.

C. Quantum dynamics of two electron scattering near critical points of the effective potential

In the previous section, we have analyzed the classical dynamics induced by the effective Hamiltonian $H_{\text{r}}^{\text{eff}}(x, y)$ in terms of individual trajectories in phase space of the relative position components x and y as the latter form a pair of canonically conjugate variables. Rigorous quantum mechanical treatment, however, is challenging as these non-commuting variables are mixed in the interaction part of the Hamiltonian, $e^2/(\kappa\sqrt{x^2 + y^2})$, in a very non-linear manner. Nevertheless, as we show below, good qualitative understanding of quantum mechanical effects in two wave packet collision can be achieved by mapping the problem onto a model Hamiltonian which on the one hand reproduces the essential properties of the original effective Hamiltonian, but in addition allows for a straightforward numerical solution.

1. Model Hamiltonian for quantum dynamics near the interaction-induced critical points

Combination of the Coulomb interaction with the beamsplitter saddle point potential in $H_{\text{r}}^{\text{eff}}(x, y)$ creates two degenerate saddle points leading to the division of the

x, y plane into four regions of topologically distinct infinite motion and a single region of the bound motion hosting quasi-stationary quantum states, see the right panel of Fig. 3. These features are present in the model double barrier Hamiltonian, which we choose to be, $y \rightarrow q$, $x \rightarrow p = -i\partial/\partial q$,

$$H^{\text{mod}}(p, q) = \frac{p^2}{2} + U(q), \quad (44)$$

$$U(q) = \frac{a^2}{\cosh(q/a - \delta)} + \frac{a^2}{\cosh(q/a + \delta)}.$$

Our mapping also reverses the sign of the potential, $H_r^{\text{eff}}(x, y) \rightarrow -H^{\text{mod}}(p, q)$, such that the bound motion segment of phase space becomes a bottom, not a top of the energy landscape. Hence, in this picture, the anti-bound molecular states correspond to quasibound states between the two barriers. We consider the barrier width a and the half-distance δ between the barriers large compared to unity. In this parameter range the dimensionless potential $U(q)$, Eq. (44), has two maxima at $q = \pm q_m \approx a\delta$ with a quadratic approximation $U = U_0 - \lambda_I^2(q \pm q_m)^2/2$ with $U_0 \rightarrow a^2$ and $\lambda_I \rightarrow 1$ for large q_m . Hence the classical trajectories near the energy U_0 , being the level lines of $H^{\text{mod}}(p, q)$, approximate the topology of trajectories of $H_r^{\text{eff}}(x, y)$, compare Fig. 8 (dotted lines in the top panel) and Fig. 3 (panel on the right). In this regime the region of finite motion supports a sufficient number of quasi-bound states as its area $\sim a\delta \gg 1$ and $[p, q] = -i$.

To characterize the original model Eqs. (13,14) in Section III we have introduced two Lyapunov exponents: $\lambda = (1/eB)\sqrt{AC}$, Eq. (17), governing the phase space dynamics for either the single electron or for the center of mass of the electron pair and $\lambda_I = (1/eB)\sqrt{3(A+C)C}$, Eq. (18), responsible for the motion on the relative coordinate plane near one of the interaction-induced saddle points. In the units of the dimensionless model Hamiltonian, Eq. (44), we have the corresponding $\lambda_I = -\partial^2 U/\partial q^2|_{q=q_m} \rightarrow 1$ for large interbarrier separation $a\delta$. Hence in the numerical examples that follow time is measured in units of approximately λ_I^{-1} .

2. Example I: Squeezing and stretching dynamics near interaction-induced saddle points

We consider the time evolution of a quantum state initialized at $t = 0$ by a Gaussian wave function,

$$\psi(q, 0) = a^{-1/2}\pi^{-1/4} \exp[-(q - q_0)^2/2a^2 + iqp_0]. \quad (45)$$

The corresponding phase space density, c.f. Eq. (32), is $\rho(p, q, 0) = \pi^{-1} \exp(-(q - q_0)^2/a^2 - (p - p_0)^2/a^2)$. The initial coordinate $q_0 = -10a$ is taken sufficiently far from the double well ($|q_0| \ll q_m$) and the initial momentum p_0 corresponds to incoming energy matching the maximum of a single barrier, $p_0^2/2 \approx U_0$.

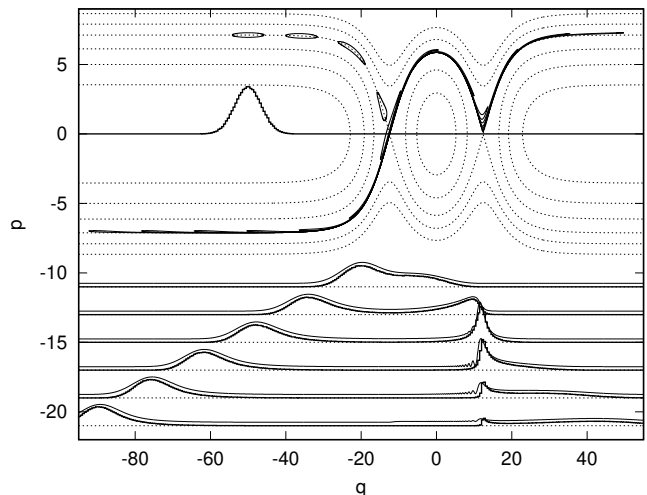


FIG. 8. Phase space dynamics induced by a double-barrier model, Eq. (44), describing the relative motion of two initially well-separated electrons. Top: Liouvillean evolution of an initially Gaussian density $\rho(q, p, t)$, traced by snapshots of the half-height contour at $t = 0, 2, \dots, 20$. Constant energy lines (dotted) guide the flow, the distribution is centered on the separatrix (resulting in equal transmission and reflection probabilities). Parameters of the potential (44) and the initial state (45) are $a = 5$, $\delta = 2.5$ and $q_0 = -10a$, $p_0 = \sqrt{2}a$, respectively. Bottom: probability density for q at six selected times $t = 10, 12, \dots, 20$ (from top to bottom), computed by projecting classically evolved phase-space density, $\rho(q, t) = \int \rho(p, q, t) dp$ (thick lines), and by solving the time-dependent Schrödinger equation, $|\psi(q, t)|^2$ (thin lines, slightly shifted upwards for comparison).

First we illustrate the Liouvillean phase space dynamics generated by $H^{\text{mod}}(p, q)$, neglecting the anti-symmetrization requirement for clarity. Figure 8 shows the evolution of an ensemble of classical trajectories with initial distribution corresponding to the Wigner representation of $\psi(q, 0)$. Like previously in Figs. 5 and 6 we consider both the density in the phase plane $\rho(p, q, t)$ and the projected density along one coordinate, $\rho(q, t) = \int \rho(p, q, t) dp$. As the Liouvillean flow preserves densities and only changes the shapes of the areas, the resulting stretching and squeezing dynamics can be traced by following the half-height level line of the initial density.

We see that after hitting the first potential barrier the density is split into the reflected part with energy below U_0 and the transmitted part with energy above U_0 without forming singular features, similar to the single saddle point in the non-interacting problem, c.f. Fig. 5. At later times the probability for a system to stay with the relative coordinate close to the first barrier decays as $e^{-\lambda_I t}$.

In contrast, in the vicinity of the second barrier (which corresponds to the second interaction-induced saddle point of the relative coordinate Hamiltonian), a singular long-lived density feature accumulates, and then slowly decays. This happens because of the trajectories leav-

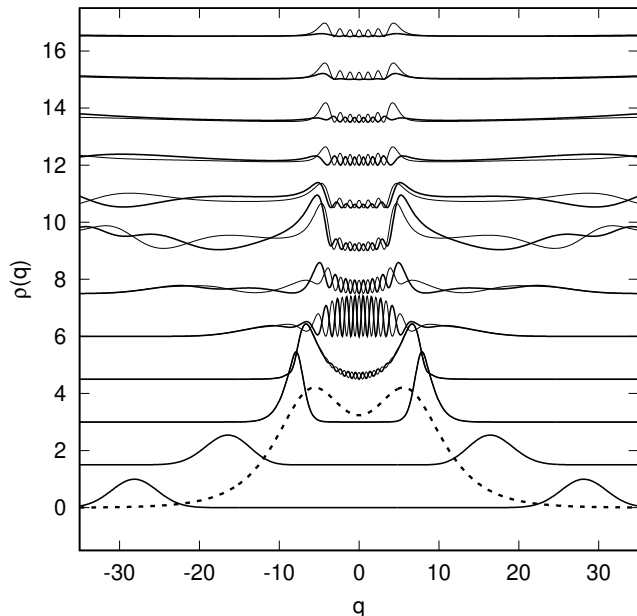


FIG. 9. Evolution of the probability density under the model Hamiltonian (44). The dashed line shows the potential $U(q)$ with parameters $a = 4$ and $\delta = 1.5$. The set of twelve continuous-line graphs shows the density profiles for $t = 2, 4, \dots, 24$ (from bottom to top) of the symmetric ($\rho(q) = |\psi_+(q, t)|^2$, thin) and antisymmetric ($\rho(q) = |\psi_-(q, t)|^2$, thick) superpositions of initially Gaussian states Eq. (46), with parameters $q_0 = -10a$ and $p_0 = 1.051 \times \sqrt{2}a$ (central energy is raised slightly to match the top of the two close barriers). The top five curves ($t \geq 16$) are multiplied by an extra factor of three.

ing the first barrier and trying to reach the second one at larger times became closer and closer to the separatrix and thus are delayed more at the second barrier. A simple analysis of stretching-squeezing behavior at two consecutive saddle points shows that the probability to find the relative coordinate close to the second stationary point decays with half the exponent $\sim e^{-\lambda t/2}$.

Additionally, we compare the statistics of the classical trajectories to the exact quantum mechanical solution for the one-dimensional density $|\psi(q, t)|^2$. The comparison in Fig. 8 show very good overall agreement, except for oscillatory features that develop between the barriers due to interference (most visible in the bottom panel at q just below $q_m \approx 12.5$). We scrutinize these uniquely quantum features in our next numerical example below.

3. Example II: Effect of exchange symmetry and formation of a quasi-bound state

In Fig. 9, we take a closer look at the snapshots of the probability density $|\psi_{\pm}(q, t)|^2$ as two electrons approach each other and undergo quantum scattering governed by the double-well model Hamiltonian Eq. (44). This time we take into account the symmetry requirements dictated

by exchange statistics and consider evolution of both orbitally symmetric (+, spin singlet) and anti-symmetric (-, spin triplet) states. The properly symmetrized initial state corresponding to the Gaussian Eq. (45) is

$$\psi_{\pm}(q, 0) \propto \left\{ \exp[-(q - q_0)^2/2a^2 + iqp_0] \pm \exp[-(q + q_0)^2/2a^2 - iqp_0] \right\}. \quad (46)$$

The sequence of density profiles in Fig. 9 illustrates the consecutive stages of the time evolution. We see two initially well-separated wave packets approaching the central interaction region, where they start to overlap and interfere. This interference appears in the form of fast oscillations with smooth envelopes over the maxima and the minima, as the two overlapping components arrive into the central region (near $|q| < |q_m|$) with opposite and large momenta $p \approx \pm p_0$.

As the propagating wave reaches the second barrier, a new standing wave pattern emerges, with the envelope of the oscillation minima dropping to almost zero (see $t \geq 10$ traces in Fig. 9). This means that both real and imaginary parts of the wave function in the central region nearly vanish and $\psi_{\pm}(q, t)$ at longer times can be represented as an almost real function multiplied by a q -independent phase factor. This wave function corresponds to a quasi-bound state with a particular number of nodes between the two barriers. Resonant excitation of such quasi-bound states, illustrated in Fig. 9, corresponds to the creation of long-lived electron molecules with well-defined energies and decay width. Quantum tunneling is essential both for excitation and, reciprocally, for the decay of these quasi-bound states with energies below U_0 . As the tunneling rates are exponentially sensitive to the confining potential barrier height, the widths of these resonances will differ by orders of magnitude, hence initially a single wave function with resonant energy close to U_0 dominates $\psi_{\pm}(q, t)$. The slowly decaying quasi-stationary density profile corresponding to one of such resonances can be clearly seen for $\psi_-(q, t)$ at $t = 20 \dots 24$. Crucially, the exchange symmetry of the wave function, $\psi_{\pm}(q, t) = \pm \psi_{\pm}(-q, t)$, plays a crucial role in selecting the excitable resonances, as one can see from the difference between ψ_- and ψ_+ at late times in Fig. 9. This is because for the symmetric double-well potential, $U(q) = U(-q)$, the parity of the (quasi)-bound one-dimensional wave functions coincides with the parity of the level number, hence the resonance conditions for ψ_+ and ψ_- with the same parameters of the initial state (46) are vastly different.

4. Example III: Quantum decay of the molecular states

We further illustrate the excitation and decay of quasi-bound two-electron states in HOM-type two electron collisions by computing the probability $I(t)$ of the pair to

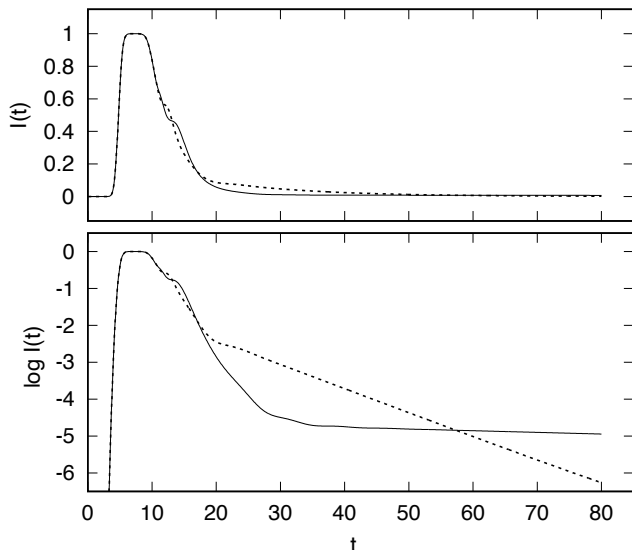


FIG. 10. Probability $I(t)$ of $|q| < q_c = 3.125a$ for the numerical solution illustrated in Fig. 9. Here the dashed lines marks the symmetric (I_+) and the solid lines — the antisymmetric (I_-) case, respectively; bottom panel depicts the same data as the top but on a logarithmic scale.

remain close as

$$I_{\pm}(t) = \int_{-q_c}^{+q_c} |\psi_{\pm}(q, t)|^2 dq. \quad (47)$$

For the numerical example analyzed in Fig. 9 where $q_m = 5.55$, we choose a cut-off distance $q_c = 3.125a = 12.5$ and plot $I_{\pm}(t)$ in Fig. 10. As the selected region is larger than the distance between the barriers and the wave packet width, the initial maximum of $I(t)$ is a plateau close to 1 as long as the whole wave packet fits into $|q| < q_0$. The initial decay after the plateau ($t \approx 10 \dots 12$) is rapid as the population is reflected classically at the first ($E < U_0$) or transmitted over the first and then the second barrier ($E > U_0$), escapes with decay rates λ_I and $\lambda_I/2$, respectively. This corresponds to the relative motion trajectories that separate without experiencing interference, as discussed in Fig. 8 and the accompanying subsection above. In Figure 10, this “classical” stage of evolution is observed up to $t \approx 12$ as two traces of opposite exchange symmetry, $I_+(t)$ and $I_-(t)$, remain close to each other.

After the classically reflected and transmitted trajectories have left, the decay of the proximity probability $I(t)$ slows down and transitions into the asymptotic regime where one expects a piece linear $\ln I(t)$, corresponding to the hierarchy of resonances,

$$I(t) \propto \sum_n \alpha_n e^{-\gamma_n t}. \quad (48)$$

As the decay rates γ_n for even and odd states are expected to differ substantially, the two traces deviate. A clear exponential behavior at long times ($t > 20$ for ‘+’

and $t > 50$ for ‘-’) is seen in Figure 10, with rates $\gamma_n = 0.064$ and 0.0046 for the symmetric and antisymmetric cases, respectively. These lifetimes are significantly longer than $\lambda_I = 0.928$.

Finally, we discuss the long-time behavior of the probability $P(t)$ to find both electrons in the beamsplitter region. This condition requires both (a) the relative distance and (b) the center of mass to stay close to the origin. The probability for (a) is proportional to $I(t)$ in the asymptotic regime of Eq. (48). The probability for (b) is $\sim e^{-\lambda t}$ as dictated by Eq. (26) in Section IV A. As the two dynamics are decoupled, this implies the product of probabilities, i.e.

$$P(t) \sim e^{-\lambda t} I(t) \sim \sum_n \alpha_n e^{-\lambda t - \gamma_n t}. \quad (49)$$

This asymptotics agrees with the factorized long-time limit, Eq. (38), of a generic initial wave function Eq. (37): the asymptotics of the center of mass wave function, $|\psi_{c.m.}(x, t)|^2 \sim e^{-\lambda t}$ is driven by the classical Lyapunov exponent λ , and the relative coordinate wave function converges to a superposition of long-lived ($\gamma_n \ll \lambda$) uniformly decaying resonance states, $\psi_r(x, t) \rightarrow \sum_n a_n \psi_n(x) e^{-\gamma_n t/2}$.

Hence we conclude that a smooth quadratic beamsplitter acts as a filter, delaying anti-bound states of electron pairs in its vicinity with a characteristic decay of the cumulative probability $P(t) \approx e^{-\lambda t}$ regardless of whether the pairs are formed by tunneling in a collision (HOM geometry, as discussed in this section) or arrive from a potential other source (HBT geometry, discussed in Section IV). The advantage of the HOM setup could be that there is a clear scenario for controlled generation of the pairs that can serve as an entanglement resource, as we outline below.

D. Creation of entangled spin-pairs in the time domain

The observation of the formation of anti-bound states with different life-times for symmetric (spin-singlet) and antisymmetric (spin-triplet) orbital wave functions provides a way to separate the formation of spin-singlets and spin triplets temporally using the HOM-geometry. We note that the spin-polarized state can only have the antisymmetric orbital wave function (cf. Eq. (33)). It has the total wave function $\Psi(x_1\sigma_1, x_2\sigma_2, t) = \psi(x_1, x_2, t)\chi_{\uparrow}(\sigma_1)\chi_{\uparrow}(\sigma_2)$. Antisymmetry for fermions requires that $\psi(x_1, x_2, t) = -\psi(x_2, x_1, t)$ and only symmetric orbital wave functions need to be considered. Here, $\chi_{\uparrow}(\sigma_i)$ is the spin wave function of electron $i = 1, 2$ assumed to be in the spin-up (\uparrow) state.

Now suppose that we inject the spin product state $|\uparrow\rangle_{S_1} |\downarrow\rangle_{S_2}$ where S_1 and S_2 refer to the two injection sources (see Fig. 1). Injection of electrons with a definite spin direction could be achieved using the spin-filtering effects of quantum dots in the Coulomb blockade regime

and subjected to a magnetic field [44]. Initially, the two electrons are well separated and localized near S_1 and S_2 , respectively. So the initial total wave function takes on the form

$$\Psi_{\text{in}}(x_1\sigma_1, x_2\sigma_2) = \frac{1}{\sqrt{2}} (\phi_{S_1}(x_1)\chi_{\uparrow}(\sigma_1)\phi_{S_2}(x_2)\chi_{\downarrow}(\sigma_2) - \phi_{S_1}(x_2)\chi_{\uparrow}(\sigma_2)\phi_{S_2}(x_1)\chi_{\downarrow}(\sigma_1)). \quad (50)$$

This wave function can be more conveniently written in second quantized form

$\Psi_{\text{in}}(x_1\sigma_1, x_2\sigma_2) = \langle x_1\sigma_1, x_2\sigma_2 | d_{S_1\uparrow}^\dagger d_{S_2\downarrow}^\dagger | 0 \rangle$ where $d_{S_i\sigma}^\dagger$ creates an electron with spin σ near source S_i , $i = 1, 2$ and $|0\rangle$ is the particle vacuum. The corresponding state ket $|\Psi_{\text{in}}\rangle = d_{S_1\uparrow}^\dagger d_{S_2\downarrow}^\dagger |0\rangle$ can be written as the sum of a $S = 0$ spin singlet $|S\rangle = (1/\sqrt{2})(d_{S_1\uparrow}^\dagger d_{S_2\downarrow}^\dagger - d_{S_1\downarrow}^\dagger d_{S_2\uparrow}^\dagger)|0\rangle$ and a $S = 1, S_z = 0$ spin triplet $|T_0\rangle = (1/\sqrt{2})(d_{S_1\uparrow}^\dagger d_{S_2\downarrow}^\dagger + d_{S_1\downarrow}^\dagger d_{S_2\uparrow}^\dagger)|0\rangle$ as

$$|\Psi_{\text{in}}\rangle = \frac{1}{\sqrt{2}} (|S\rangle + |T_0\rangle) \quad (51)$$

To make contact with our discussion about the form of the wave function, we note that

$$\begin{aligned} \langle x_1\sigma_1, x_2\sigma_2 | S, T_0 \rangle &= \frac{1}{\sqrt{2}} (\chi_{\uparrow}(\sigma_1)\chi_{\downarrow}(\sigma_2) \mp \chi_{\uparrow}(\sigma_2)\chi_{\downarrow}(\sigma_1)) \\ &\times \frac{1}{\sqrt{2}} (\phi_{S_1}(x_1)\phi_{S_2}(x_2) \pm \phi_{S_1}(x_2)\phi_{S_2}(x_1)), \quad (52) \end{aligned}$$

with upper (lower) sign for S (T_0). As \mathbf{S}^2 and S_z commute with H , the singlet and triplet parts of the wave function $\Psi_{\text{in}}(x_1\sigma_1, x_2\sigma_2)$ are conserved during the time evolution and when approaching each other at the beamsplitter. As the orbital part of the wave function will separate in a center of mass and relative coordinate part at long times we have $\psi(x_1, x_2, t) = \psi_r(x, t)\psi_{\text{cm}}(X, t)$ (cf. Eq. (35)) with $\psi_r^{S, T_0}(x, t) = \pm \psi_r^{S, T_0}(-x, t)$ for the singlet part (+ sign) and triplet part (- sign). Since time evolution is governed by a linear operator $|\Psi_{\text{out}}(t)\rangle = \exp(-iHt/\hbar)|\Psi_{\text{in}}\rangle$, we have

$$|\Psi_{\text{out}}(t)\rangle = \frac{1}{\sqrt{2}} (|S(t)\rangle + |T_0(t)\rangle). \quad (53)$$

The probability density that two electrons are detected in a singlet state at corresponding detectors D_1 and D_2 during a time interval Δt around time t is

$$\begin{aligned} P_D^S(t, \Delta t) &= \frac{1}{2} \int_{t-\Delta t/2}^{t+\Delta t/2} dt' \langle S(t') | (|x_{D_1}, x_{D_2}\rangle \langle x_{D_1}, x_{D_2}| \\ &\quad + |x_{D_2}, x_{D_1}\rangle \langle x_{D_2}, x_{D_1}|) | S(t') \rangle \\ &= \int_{t-\Delta t/2}^{t+\Delta t/2} dt' |\psi_r^S(|x_{D_1} - x_{D_2}|, t')|^2 \\ &\quad \times |\psi_{\text{cm}}^S((x_{D_1} + x_{D_2})/2, t')|^2, \quad (54) \end{aligned}$$

and for $P_D^{T_0}(t, \Delta t)$ correspondingly. Note that at long times t , as discussed in Subsections V C 3. and 4., the probability to stay close to the beamsplitter region is ruled by quantum tunneling into the anti-bound states. Even though the survival probability is diminished for the center of mass coordinate being still at the center by an exponential decay $e^{-\lambda t}$ (see Fig. 7), the relative wave function undergoes quantum tunneling through anti-bound states with different lifetimes for singlet and triplet states (see Fig. 10). For two electrons observed at different detectors D_1 and D_2 , the relative coordinate needs to have tunneled out of the molecule. For the specific example shown in Fig. 10, this is much more likely for the singlet as for the triplet in the time range where the most coupled state dominates the decay ($t = 30 \dots 40$). Therefore, detection of delocalized entanglement becomes possible.

Coincident late arrival of electrons to two detectors selects for a spin-entangled state such that a choice between a singlet or a triplet can be tuned by tuning the beamsplitter potential and choosing the appropriate time delay for detection. On a related note, tunable loading of stable singlets or triplets in a quantum dot based on tunneling rate separation [45] and coherent transport of entangled electron spin pairs over several μm [46] have been recently demonstrated. Hence the two-electron collider can serve as stochastic source of mobile EPR pairs, i.e. the two electrons are separated in (orbital) space to two distant detectors but still correlated in the spin degree of freedom. The detection of such spin-correlations could be achieved via a Bell test using tunable spin filters combined with charge noise measurements [47–49].

VI. CONCLUSIONS

We have analyzed the problem of two interacting electrons scattering at a saddle point potential in the quantum Hall regime. By introducing canonically conjugate guiding centers for the drift motion in two dimensions the problem reduces to that of two electrons interacting via strong long-range Coulomb interaction and subjected to the saddle point potential. We have shown that the problem remains exactly separable in relative and center-of-mass coordinates. These coordinates are well suited to describe effects of anti-bound states of electron pairs in the scattering problem of Hanbury Brown and Twiss and Hong-Ou-Mandel setups of electron optics. Our focus lies on the study of critical trajectories where two injected electrons stay for a long time at the beamsplitter. We found characteristic long-time tails for the corresponding probabilities using classical phase space arguments as well as quantum mechanical effects of the two-particle problem. This leads to the information about the beamsplitter potential, the nature of the interaction between two electrons as well as to the characteristic tendency to form quasi-bound states. The latter effect is shown to be different for symmetric and antisymmetric orbital wave

functions distinguishing spin-singlets from spin-triplets. Our results may motivate experiments in the field of two-particle quantum optics with a time-resolved detection scheme.

ACKNOWLEDGMENTS

We are thankful for insightful discussions with P. W. Brouwer. PS and PR acknowledge support from the Deutsche Forschungsgemeinschaft (DFG, German Research Foundation) under Germany's Excellence Strategy – EXC-2123 QuantumFrontiers – 390837967. VK has been supported by grant no. lzp-2021/1-0232 from the Latvian Council of Science and the Latvian Quantum Initiative within European Union Recovery and Resilience Facility project no. 2.3.1.1.i.0/1/22/I/CFLA/001.

Appendix: Analytical derivations

Trajectories asymptotics. Before considering the specific critical examples, like Eqs. (40) and (41), we need to describe the asymptotics of generic trajectories in the HOM setup at the parabolic beamsplitter.

Individual electron's trajectories are found straightforwardly from the relative coordinate and the center of mass trajectories. The generic relative coordinate trajectory described by the effective Hamiltonian H_r^{eff} , Eqs. (14) may be chosen to be symmetric in time with the asymptotics

$$\begin{aligned} x(\lambda|t| \gg 1) &= -\frac{\alpha_r}{\sqrt{A}}e^{\lambda|t|} - \frac{\beta_r}{\sqrt{A}}e^{-\lambda|t|}, \\ y(\lambda|t| \gg 1) &= -\frac{t}{|t|}\frac{\alpha_r}{\sqrt{C}}e^{\lambda|t|} + \frac{t}{|t|}\frac{\beta_r}{\sqrt{C}}e^{-\lambda|t|}, \end{aligned} \quad (\text{A.1})$$

with arbitrary coefficients α_r, β_r . At very large $\lambda|t|$ (either for negative or positive times t) the first term $\sim \alpha_r$ in Eqs. (A.1), describing the drift along the separatrix, dominates. The second $\sim \beta_r$ term in Eqs. (A.1) describes the asymptotic squeezing of the trajectories around the separatrix. Taking into account these terms would allow us to find the electrons' energies before and after collision.

Together with the proper redefinition of the zero of time, $t = 0$, Eqs. (A.1) describe all the relative coordinate trajectories except two. The two remaining critical trajectories are those where one starts with a very large displacement (either at the upper left, or the lower right corners of the (x, y) plane in our example), but then the two electrons stay almost frozen, asymptotically approaching one of the stationary points $(x, y) = (0, \pm 2y_0)$. Knowing the trajectories with the inter-electron distance frozen at $t \rightarrow \infty$ is necessary for deriving Eq. (40). The negative time asymptotics of these critical trajectories is

still given by Eqs. (A.1) with the product of the coefficients $\alpha_r\beta_r$ having a unique value (to be found below).

The center of mass classical trajectory described by the quadratic in coordinates effective Hamiltonian $H_{\text{cm}}^{\text{eff}}$, Eq. (13), may be found exactly

$$\begin{aligned} X(t) &= \frac{\alpha_{\text{cm}}}{\sqrt{A}}e^{-\lambda t} - \frac{\beta_{\text{cm}}}{\sqrt{A}}e^{\lambda t}, \\ Y(t) &= -\frac{\alpha_{\text{cm}}}{\sqrt{C}}e^{-\lambda t} - \frac{\beta_{\text{cm}}}{\sqrt{C}}e^{\lambda t}. \end{aligned} \quad (\text{A.2})$$

Here again $\alpha_{\text{cm}}, \beta_{\text{cm}}$ are two arbitrary coefficients.

Next, using that the classical single-electron energies are $\varepsilon_i = -Ax_i^2/2 + Cy_i^2/2$, $i = 1, 2$, with the help of Eqs. (A.1, A.2) we find the energies of electrons before the collision, at negative times $\lambda t \ll -1$

$$\varepsilon_{1(2)\text{in}} = \alpha_{\text{cm}}\beta_{\text{cm}} \pm [\alpha_{\text{cm}}\beta_r - \beta_{\text{cm}}\alpha_r] - \alpha_r\beta_r/4, \quad (\text{A.3})$$

and after the collision, at $\lambda t \gg 1$,

$$\varepsilon_{1(2)\text{out}} = \alpha_{\text{cm}}\beta_{\text{cm}} \pm [\alpha_{\text{cm}}\alpha_r - \beta_{\text{cm}}\beta_r] - \alpha_r\beta_r/4. \quad (\text{A.4})$$

Here in both cases in/out the upper sign (+) is for electron 1 and the lower sign (−) for electron 2.

The time shifts between the ingoing and outgoing electrons, Δt_{in} and Δt_{out} , are found as

$$\begin{aligned} x_1(t)/x_2(t) &\underset{t \rightarrow -\infty}{=} -e^{-\lambda\Delta t_{\text{in}}}, \\ x_1(t)/x_2(t) &\underset{t \rightarrow +\infty}{=} -e^{\lambda\Delta t_{\text{out}}}. \end{aligned} \quad (\text{A.5})$$

Using $y_{1,2}$ instead of $x_{1,2}$ would obviously be the same. From Eqs. (A.1, A.2) we deduce

$$e^{\lambda\Delta t_{\text{in}}} = \frac{\alpha_r + 2\alpha_{\text{cm}}}{\alpha_r - 2\alpha_{\text{cm}}}, \quad e^{\lambda\Delta t_{\text{out}}} = \frac{\alpha_r + 2\beta_{\text{cm}}}{\alpha_r - 2\beta_{\text{cm}}}. \quad (\text{A.6})$$

Derivation of Eq. (40): We are searching for a special solution of the equations of motion where two electrons with the initial energies $\varepsilon_{1\text{in}}, \varepsilon_{2\text{in}}$ enter the beamsplitter with the time delay Δt_{in} and stay there forever, approaching asymptotically the stationary positions $(x, y) = (0, \pm 2y_0)$. This means choosing the solution Eqs. (A.2) with $\beta_{\text{cm}} = 0$. The coefficient α_{cm} remains undetermined. Varying α_{cm} leads to the time shift of the trajectory, $\alpha_{\text{cm}} > 0$ means the electron 1 coming from the left enters the beamsplitter first.

The relation between the coefficients α_r and β_r for the critical trajectory with stationary relative coordinate after the collision is found from its energy $-Ax^2/4 + Cy^2/4 = 2\varepsilon_0$ (see H_r^{eff} , Eq. (14)), yielding

$$\beta_r\alpha_r = -2\varepsilon_0. \quad (\text{A.7})$$

Finally, the first of Eqs. (A.6) may be written as

$$\alpha_{\text{cm}} = \tanh(\lambda\Delta t_{\text{in}}/2)\frac{\alpha_r}{2}. \quad (\text{A.8})$$

Substituting the last two results into Eq. (A.3) yields Eq. (40).

Towards derivation of Eq. (41): Now we want to consider the case of injection of two electrons with non-interacting half transmission energies $\varepsilon_{1\text{in}} = \varepsilon_{2\text{in}} = 0$ but with a finite time delay Δt_{in} . Mathematically that means $\beta_r = \beta_{\text{cm}} = 0$ and arbitrary α_{cm} . The remaining coefficient may be written in a form

$$\alpha_r = \sqrt{2\gamma_0\varepsilon_0}. \quad (\text{A.9})$$

The purely numerical coefficient $\gamma_0 \sim 1$ here depending on the ratio A/C , could not be found with the simple considerations presented here. Nevertheless, it may be extracted from the exact solutions of equations of motion developed in [28], $\gamma_0 = 2[2A/(A+C)]^{1/3}/3$. Combining Eqs. (A.4,A.8,A.9) yields Eq. (41).

-
- [1] E. Bocquillon, V. Freulon, F. D. Parmentier, J.-M. Berroir, B. Plaais, C. Wahl, J. Rech, T. Jonckheere, T. Martin, C. Grenier, D. Ferraro, P. Degiovanni, and G. Feve, Electron quantum optics in ballistic chiral conductors, *Annalen der Physik* **526**, 1 (2014).
- [2] C. Bauerle, D. Christian Glatzli, T. Meunier, F. Portier, P. Roche, P. Roulleau, S. Takada, and X. Waintal, Coherent control of single electrons: a review of current progress, *Reports on Progress in Physics* **81**, 056503 (2018).
- [3] M. Henny, S. Oberholzer, C. Strunk, T. Heinzel, K. Ensslin, M. Holland, and C. Schonenberger, The Fermionic Hanbury Brown and Twiss Experiment, *Science* **284**, 296 (1999).
- [4] W. D. Oliver, J. Kim, R. C. Liu, and Y. Yamamoto, Hanbury Brown and Twiss-Type Experiment with Electrons, *Science* **284**, 299 (1999).
- [5] G. Feve, A. Mahe, J.-M. Berroir, T. Kontos, B. Plaais, D. C. Glatzli, A. Cavanna, B. Etienne, Y. Jin, G. Feve, A. Mahe, J.-M. Berroir, T. Kontos, B. Placais, D. C. Glatzli, A. Cavanna, B. Etienne, and Y. Jin, An on-demand coherent single-electron source., *Science* **316**, 1169 (2007).
- [6] E. Bocquillon, F. D. Parmentier, C. Grenier, J.-M. Berroir, P. Degiovanni, D. C. Glatzli, B. Plaais, A. Cavanna, Y. Jin, and G. Feve, Electron Quantum Optics: Partitioning Electrons One by One, *Physical Review Letters* **108**, 196803 (2012).
- [7] E. Bocquillon, V. Freulon, J.-M. Berroir, P. Degiovanni, B. Plaais, A. Cavanna, Y. Jin, and G. Feve, Coherence and indistinguishability of single electrons emitted by independent sources., *Science* **339**, 1054 (2013).
- [8] T. Jullien, P. Roulleau, B. Roche, A. Cavanna, Y. Jin, and D. C. Glatzli, Quantum tomography of an electron., *Nature* **514**, 603 (2014).
- [9] R. Bisognin, A. Marguerite, B. Roussel, M. Kumar, C. Cabart, C. Chapdelaine, A. Mohammad-Djafari, J.-M. Berroir, E. Bocquillon, B. Plaais, A. Cavanna, U. Gennser, Y. Jin, P. Degiovanni, and G. Feve, Quantum tomography of electrical currents, *Nature Communications* **10**, 3379 (2019).
- [10] B. Roussel, C. Cabart, G. Feve, and P. Degiovanni, Processing Quantum Signals Carried by Electrical Currents, *PRX Quantum* **2**, 020314 (2021).
- [11] W. D. Oliver, F. Yamaguchi, and Y. Yamamoto, Electron entanglement via a quantum dot, *Physical Review Letters* **88**, 037901 (2002).
- [12] D. S. Saraga, B. L. Altshuler, D. Loss, and R. M. Westervelt, Coulomb scattering in a 2d interacting electron gas and production of epr pairs, *Physical Review Letters* **92**, 246803 (2004).
- [13] D. S. Saraga, B. L. Altshuler, D. Loss, and R. M. Westervelt, Coulomb scattering cross section in a two-dimensional electron gas and production of entangled electrons, *Physical Review B* **71**, 045338 (2005).
- [14] A. Schroer, B. Braunecker, A. Levy Yeyati, and P. Recher, Detection of spin entanglement via spin-charge separation in crossed tomonaga-luttinger liquids, *Physical Review Letters* **113**, 266401 (2014).
- [15] S. Ryu and H.-S. Sim, Partition of Two Interacting Electrons by a Potential Barrier, *Physical Review Letters* **129**, 166801 (2022).
- [16] C. Leicht, P. Mirovsky, B. Kaestner, F. Hohls, V. Kashcheyevs, E. V. Kurganova, U. Zeitler, T. Weimann, K. Pierz, and H. W. Schumacher, Generation of energy selective excitations in quantum Hall edge states, *Semiconductor Science and Technology* **26**, 055010 (2011).
- [17] J. D. Fletcher, P. See, H. Howe, M. Pepper, S. P. Giblin, J. P. Griffiths, G. A. C. Jones, I. Farrer, D. A. Ritchie, T. J. B. M. Janssen, and M. Kataoka, Clock-Controlled Emission of Single-Electron Wave Packets in a Solid-State Circuit, *Physical Review Letters* **111**, 216807 (2013).
- [18] N. Ubbelohde, F. Hohls, V. Kashcheyevs, T. Wagner, L. Fricke, B. Kastner, K. Pierz, H. W. Schumacher, and R. J. Haug, Partitioning of on-demand electron pairs, *Nature Nanotechnology* **10**, 46 (2015).
- [19] J. Waldie, P. See, V. Kashcheyevs, J. P. Griffiths, I. Farrer, G. A. C. Jones, D. A. Ritchie, T. J. B. M. Janssen, and M. Kataoka, Measurement and control of electron wave packets from a single-electron source, *Physical Review B* **92**, 125305 (2015).
- [20] M. Kataoka, N. Johnson, C. Emary, P. See, J. P. Griffiths, G. A. C. Jones, I. Farrer, D. A. Ritchie, M. Pepper, and T. J. B. M. Janssen, Time-of-Flight Measurements of Single-Electron Wave Packets in Quantum Hall Edge States, *Physical Review Letters* **116**, 126803 (2016).
- [21] L. Freise, T. Gerster, D. Reifert, T. Weimann, K. Pierz, F. Hohls, and N. Ubbelohde, Trapping and Counting Ballistic Nonequilibrium Electrons, *Physical Review Letters* **124**, 127701 (2020).
- [22] B. Kaestner and V. Kashcheyevs, Non-adiabatic quantized charge pumping with tunable-barrier quantum dots: a review of current progress, *Reports on Progress in Physics* **78**, 103901 (2015).
- [23] S. P. Giblin, A. Fujiwara, G. Yamahata, M.-H. Bae, N. Kim, A. Rossi, M. Mottonen, and M. Kataoka, Evidence for universality of tunable-barrier electron pumps, *Metrologia* **56**, 044004 (2019).
- [24] D. Reifert, M. Kokainis, A. Ambainis, V. Kashcheyevs, and N. Ubbelohde, A random-walk benchmark for single-

- electron circuits, *Nature Communications* **12**, 285 (2021).
- [25] M. Kataoka, J. D. Fletcher, and N. Johnson, Time-resolved single-electron wave-packet detection, *physica status solidi (b)* **254**, 1600547 (2017).
- [26] J. D. Fletcher, N. Johnson, E. Locane, P. See, J. P. Griffiths, I. Farrer, D. A. Ritchie, P. W. Brouwer, V. Kashcheyevs, and M. Kataoka, Continuous-variable tomography of solitary electrons, *Nature Communications* **10**, 5298 (2019).
- [27] E. Locane, P. W. Brouwer, and V. Kashcheyevs, Time-energy filtering of single electrons in ballistic waveguides, *New Journal of Physics* **21**, 093042 (2019).
- [28] E. Pavlovska, P. G. Silvestrov, P. Recher, G. Barinovs, and V. Kashcheyevs, Collision of two interacting electrons on a mesoscopic beam splitter: Exact solution in the classical limit, *Physical Review B* **107**, 165304 (2023).
- [29] N. Ubbelohde, L. Freise, E. Pavlovska, P. G. Silvestrov, P. Recher, M. Kokainis, G. Barinovs, F. Hohls, T. Weimann, K. Pierz, and V. Kashcheyevs, Two electrons interacting at a mesoscopic beam splitter, *Nature Nanotechnology* **18**, 733 (2023).
- [30] J. D. Fletcher, W. Park, S. Ryu, P. See, J. P. Griffiths, G. A. C. Jones, I. Farrer, D. A. Ritchie, H.-S. Sim, and M. Kataoka, Time-resolved Coulomb collision of single electrons, *Nature Nanotechnology* **18**, 727 (2023).
- [31] J. D. Fletcher, W. Park, P. See, J. P. Griffiths, G. A. C. Jones, I. Farrer, D. A. Ritchie, H. S. Sim, and M. Kataoka, Coulomb sensing of single ballistic electrons, [arXiv:2412.15789](https://arxiv.org/abs/2412.15789) (2024).
- [32] R. B. Laughlin, Quantized motion of three two-dimensional electrons in a strong magnetic field, *Physical Review B* **27**, 3383 (1983).
- [33] R. B. Laughlin, Anomalous Quantum Hall Effect: An Incompressible Quantum Fluid with Fractionally Charged Excitations, *Physical Review Letters* **50**, 1395 (1983).
- [34] H. A. Fertig and B. I. Halperin, Transmission coefficient of an electron through a saddle-point potential in a magnetic field, *Physical Review B* **36**, 7969 (1987).
- [35] To characterize the curvature of the potential both experimental [20] and theoretical [34] papers often introduce the harmonic-oscillator-like frequency. That means Eq. (3) became $V(x, y) = \frac{m}{2}(\omega_y^2 y^2 - \omega_x^2 x^2)$ with obvious translation rules $A = m\omega_x^2$, $C = m\omega_y^2$.
- [36] B. Huckestein, Scaling theory of the integer quantum Hall effect, *Reviews of Modern Physics* **67**, 357 (1995).
- [37] C. Emary, L. A. Clark, M. Kataoka, and N. Johnson, Energy relaxation in hot electron quantum optics via acoustic and optical phonon emission, *Physical Review B* **99**, 045306 (2019).
- [38] M. Hillery, R. O’Connell, M. Scully, and E. Wigner, Distribution functions in physics: Fundamentals, *Physics Reports* **106**, 121 (1984).
- [39] K. Husimi, Miscellanea in Elementary Quantum Mechanics, II, *Progress of Theoretical Physics* **9**, 381 (1953).
- [40] H.-W. Lee, Theory and application of the quantum phase-space distribution functions, *Physics Reports* **259**, 147 (1995).
- [41] D. Heim, W. Schleich, P. Alsing, J. Dahl, and S. Varro, Tunneling of an energy eigenstate through a parabolic barrier viewed from Wigner phase space, *Physics Letters A* **377**, 1822 (2013).
- [42] In terms of the dimensionless function used in Refs. 28 and 29, one has $\Phi_k = E_+/(2\gamma_0\varepsilon_0)$ for $|\Phi_k| \ll 1$ with $E_+ = \varepsilon[1 + \cosh(\lambda\Delta t_{in})]$ if $\varepsilon = \varepsilon_{1in} = \varepsilon_{2in}$.
- [43] Note that a change in energy leads to a logarithmic time shift even for one non-interacting electron as this is a basic dispersion property of an energy-selective beamsplitter (see Section IV above and Sec. III-C of Ref. 28).
- [44] P. Recher, E. V. Sukhorukov, and D. Loss, Quantum dot as spin filter and spin memory, *Physical Review Letters* **85**, 1962 (2000).
- [45] T. Wenz, J. Klochan, F. Hohls, T. Gerster, V. Kashcheyevs, and H. W. Schumacher, Quantum dot state initialization by control of tunneling rates, *Physical Review B* **99**, 201409 (2019).
- [46] B. Jadot, P.-A. Mortemousque, E. Chanrion, V. Thiney, A. Ludwig, A. D. Wieck, M. Urdampilleta, C. Bäuerle, and T. Meunier, Distant spin entanglement via fast and coherent electron shuttling, *Nature Nanotechnology* **16**, 570 (2021).
- [47] S. Kawabata, Test of bell’s inequality using the spin filter effect in ferromagnetic semiconductor microstructures, *Journal of the Physical Society of Japan* **70**, 1210 (2001).
- [48] N. M. Chtchelkatchev, G. Blatter, G. B. Lesovik, and T. Martin, Bell inequalities and entanglement in solid-state devices, *Physical Review B* **66**, 161320 (2002).
- [49] P. Recher, D. S. Saraga, and D. Loss, Creation and detection of mobile and non-local spin-entangled electrons, in *Fundamental Problems of Mesoscopic Physics: Interactions and Decoherence*, edited by I. V. Lerner, B. L. Altshuler, and Y. Gefen (Springer Netherlands, Dordrecht, 2004) pp. 179–202.